Experimental investigation and semi-empirical modeling of snowflake melting

Boris Aguilar, Pierre Trontin, Kilian Köbschall, Fabien Dezitter, Jeanette Hussong, Philippe Villedieu

Experimental investigation and semi-empirical modeling of snowflake melting

Boris Aguilar[a,c,*], Pierre Trontin[b], Kilian Köbschall[d], Fabien Dezitter[a], Jeanette Hussong[d], Philippe Villedieu[c]

[a] *Airbus Helicopters S.A.S., Aéroport International Marseille Provence, Marignane, 13725, , France*
[b] *Univ Lyon, Univ Claude Bernard Lyon 1, CNRS, Ecole Centrale de Lyon, INSA Lyon, LMFA, UMR5509, 43 Bd du 11 Novembre 1918, Villeurbanne, 69622, , France*
[c] *ONERA/DMPE, Université de Toulouse, Toulouse, F-31055, , France*
[d] *Institute of Fluid Mechanics and Aerodynamics, Technische Universität Darmstadt, Alarich-Weiss-Straße 10, Darmstadt, 64287, , Germany*

Abstract

The melting process is studied for the case of snowflakes of aggregate type. Snowflakes are placed in the center of an acoustic levitator with a warm air flow. The evolution of the shape of the snowflake is recorded over time by a camera and the total melting time is measured. A model is proposed to describe the melting process. It is based on a simplified 3D geometric representation of the snowflake (spheroidal shape for the convex hull) and an accurate estimation of its bulk density throughout the melting process. This allows taking into account the very important change of the shape of the aggregate during the melting step and thus to be able to predict the total melting time with a much better accuracy than the existing models.

Keywords: Snow aggregate, melting, bulk density reconstruction.

1. Introduction

Aircraft icing has been studied since the early 20th century as a major meteorological hazard during flight. In the 1990s, ice crystal icing was identified [1], and regulations were changed accordingly. More recently, the study of snowflake

∗. Corresponding author (boris.aguilar@onera.fr)

accretion icing has been of great interest to the lower flying aircraft industry such as helicopters. Indeed, service history has shown that in-flight snow conditions have caused power interruptions on some engines with air inlets that have plenums, reverse flow, or particle separation design features. To comply with certification requirements, manufacturers must prove that each engine and its air intake system can operate throughout the engine's flight power range in snow. The ability to perform physical engine tests in icing wind tunnels being very expensive with limited capability to reproduce snow conditions, numerical tools capable of accurately predicting icing in snowy conditions are an important asset to support the development and certification of new engines and aircrafts. Consequently, a need has arisen to improve the modeling of icing with snow particles, focusing on the transport phase of the snowflake by the airflow, its impact with an aeronautical surface (wing, blade, air intake, probe, etc.) and the accretion process.

Contrary to ice crystals where high bulk densities are observed (typically of the order of 917 $\mathrm{kg.m^{-3}}$) with non-spherical but fairly regular geometric shapes, snowflakes are highly non-regular particles with a large variability in particle shape and bulk density. This is suggested by the seminal work of Nakaya [2] on the morphological properties of crystals formed by vapour deposition (see Pruppacher *et al.* [3] for a review). Using a MASC (Multi Angle Snowflake Camera) device, Praz *et al.* [4] observed thousands of ground snowflakes during the 2015/2016 winter snow events at an altitude of 2500 m on the site of Davos in Switzerland, as well as on the French Antarctic base of Dumont d'Urville. A new classification containing six categories of snowflakes was drawn from these campaigns stating that snow aggregates are the most observed category during snow events.

Many studies have been carried out in the context of the transport [5, 6], impact [7, 8] and accretion [9, 10] of ice crystals. Regarding the melting of ice particles, the pioneering work of Mason [11] consists of a simple one-dimensional model for the melting of falling solid ice spheres and graupel particles covered by a layer of liquid water. Based on this work, Villedieu [12] and Hauk [5] proposed

an extension of this model to non-spherical particles by using a generalization of the Frossling correlation [13]. They introduced the particle sphericity in the formulations of the Nusselt and Sherwood numbers to account for the influence of the particle shape in the heat and mass transfers respectively. Experiments by Hauk *et al.* [5] have shown that this model can be used to predict the total melting time of non-spherical ice particles with a rather high bulk density. However, these ice particles were collected from the walls of a chest freezer leading to particles whose geometrical characteristics are far from those of a snowflake like an aggregate (with regards to size, shape and bulk density). In [14], the effect of non-spherical particle rotation on both particle trajectory and melting behavior is studied. Snowflake melting was also studied by Matsuo *et al.* [15] by attaching the snowflake to a nylon net. This procedure allows a stable positioning and orientation of the snowflake, but the presence of the fiber affects the melting behavior and especially the spatial distribution of the melted water. Mitra *et al.* [16] studied the melting of snowflakes in a vertical cloud tunnel where the melting of natural and laboratory-made aggregates was studied under free-fall conditions. Falling snowflakes experienced warming rates comparable to those encountered in the atmosphere (on the order of 1.25 °C per 100 m). A theoretical model using an idealized oblate spheroid snowflake for the melting process was derived from these experiments [16] .

Figure 1 is an illustration of the melting process for an initially dry snowflake as described by Mitra *et al.* [16]. It can be broken down into the following stages, from $t = 0$ to $t = t_m$ where t_m corresponds to the moment when the particle is fully melted with a spherical shape :

1. From $t = 0$ to $t = 0.1t_m$ (Stage I), a significant accumulation of water appears on the outer branches of the snowflake.
2. From $t = 0.1t_m$ to $t = 0.25t_m$ (Stage II), the melt water starts to migrate from the outside of the snowflake branches to the inner part of the snowflake. During this stage, the meltwater concentrates to the connections of the snowflake branches.

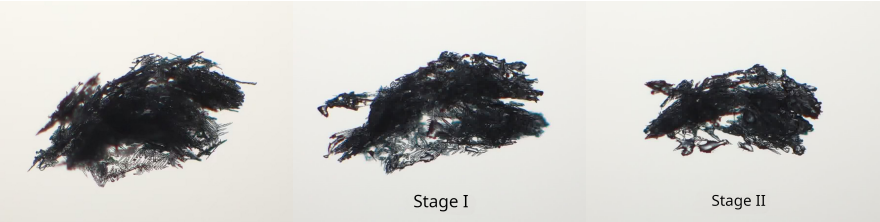

(a) $t = 0$ (b) $t = 0.10\ t_m$ (c) $t = 0.25\ t_m$

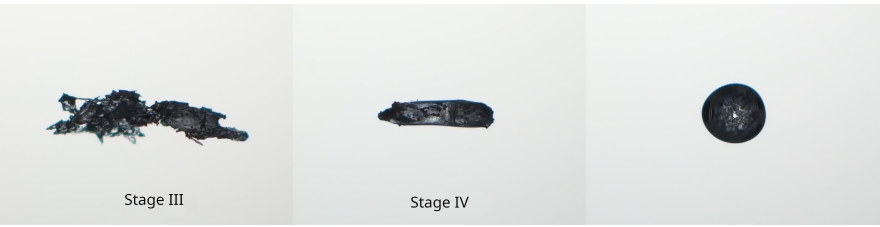

(d) $t = 0.30\ t_m$ (e) $t = 0.40\ t_m$ (f) $t = t_m$

FIGURE 1: Successive stages observed during the melting of a snowflake according to Mitra *et al.* [16]. The melting time t_m corresponds to a fully melted particle with a spherical final shape.

3. From $t = 0.25t_m$ to $t = 0.3t_m$ (Stage III), the small peripheral branches melted whereas the main branches inside the snowflake start to melt, collecting the main flow of melted water with the onset of a collapse of the snowflake structure on itself. This causes some structural rearrangements leading to a sharp decrease in the surface area of the snowflake (Fig. 1d).
4. At the end of stage IV ($t = 0.4t_m$) the peripheral structure of the snowflake completely collapsed on itself leading to an ellipsoidal structure composed of a mixture of liquid water and solid ice (Fig. 1e).
5. From $t = 0.4t_m$ to $t = t_m$, the liquid mass fraction inside the particle increases during the melting process until it reaches the value of 1. The particle is then spherical (Fig. 1f).

Mitra's experimental results (Fig. 1), supported by our own experimental results (see next part of the paper) show that the melting process of a snowflake leads to a very important change of its geometry and consequently of its exchange surface with the air. To model this process correctly, it is necessary to have a model able to take into account the influence of the complex geometry of the snowflake on the heat flux exchanged with the air, and to account for the evolution of the geometry during the melting process. This is what we propose to do in the rest of the paper.

If we restrict ourselves to simple models with at most three parameters related to the geometry of the particle, two types of models are possible :

— Type I : the *ice core density based models*. In this type of model, the assumed shape of the snowflake is not explicit. Its size is characterized by its volume equivalent diameter $d_V = (6V/\pi)^{1/3}$, which corresponds to the diameter of the sphere of the same volume V. The shape is taken into account through the sphericity of the particle defined by $\Phi = \pi d_V^2/A$ where A is the area of the particle. The volume $\pi d_V^3/6$ being by definition the true volume of the particle, the core density of the particle defined by $\rho_p^{\text{core}} = m_p/V$, m_p being the particle mass, is in this case very close to the ice density $\rho_s \approx 917$ kg.m^{-3} (provided that we can neglect the

porosity of the particle). We thus have the following relation between the mass of the particle and its diameter : $m_p = \rho_s \pi d_V^3/6$.

— Type II : the *ice bulk density based models*. In this type of model, the snowflake is represented geometrically by an oblate or prolate spheroid which corresponds to the closest spheroid that envelops the real snowflake. In the case where only a 2D image of the particle is available, this choice is arbitrary or based on an a priori knowledge of the real 3D shape. From a mathematical point of view, the spheroid is entirely characterized by two parameters : its semi-major axis a and its eccentricity e (or equivalently its sphericity). Its volume $V_\star$ corresponds only to the apparent volume of the snowflake, its real volume V being in general much smaller. To relate the mass of the snowflake to its apparent volume, it is therefore necessary to introduce the notion of bulk density of the particle defined by : $\rho_p^{\text{bulk}} = m_p/V_\star$, which by definition will be in general strictly lower than ρ_s.

The model proposed in [5] to predict the melting time of non-spherical ice particles belongs to the first category (Type I) and that proposed by Mitra [16] to the second (Type II). It is important to note that the second type of model offers an additional degree of freedom through the bulk density of the particle. This one allows taking into account the difference between the apparent volume of the snowflake (that of the enveloping spheroid) and its real volume. For Type II models, the deviation of the snowflake from the spherical shape is accounted for by two parameters, namely the eccentricity e of the enveloping spheroid, and the ratio $\rho_p^{\text{bulk}}/\rho_s$.

In this paper we show that from the experimentally obtained 2D images of a levitating and melting snowflake, it is possible to estimate its bulk density. This data allows us to construct a semi-empirical law that relates the bulk density to the fraction of liquid water Y_l of the snowflake. This law constitutes the essential brick to close the equations modeling the evolution of the liquid fraction and the apparent diameter $d_{V_\star}$ of the snowflake during the melting process. In order to evaluate the gain in accuracy brought by this new approach, we also

present in the paper a comparison between the experimental melting times and the predictions provided by Mitra's model and the core density based model proposed in [5] and already mentioned above.

In a first section (Sec. 2), the experimental apparatus is described. It consists of an acoustic levitator in which the melting of a snowflake is studied. In a second section (Sec. 3), image post-processing for particle characterization is presented. Melting models for snowflakes are detailed in Sec. 4. They are assessed and discussed in Sec. 5. Finally, conclusions are drawn.

2. Melting experiments : apparatus description

The core of the experimental setup is the acoustic levitator (Fig. 2) [5], which enables levitating the investigated snowflake in an airflow. This acoustic

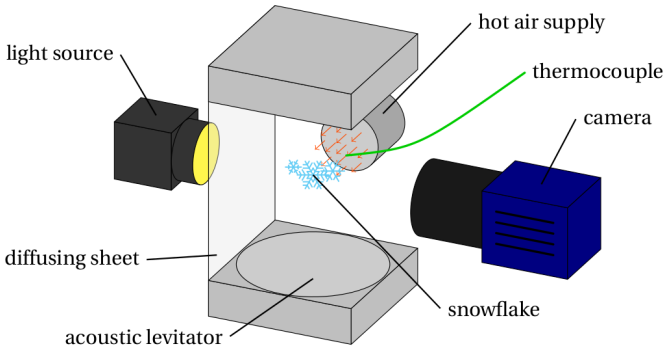

FIGURE 2: Schematic of the experimental setup consisting of a snowflake in an acoustic levitator, hot air supply, a thermocouple, a light source and a camera. The hot air blower upstream of the illustrated pipe is not shown here.

levitator is placed in a chest freezer. A hot air blower is positioned outside of the chest freezer and blows warm air in a pipe that directs the air to the levitating snowflake. The air speed is measured once for each experimental run. The temperature is measured by a thermocouple that is positioned directly in front of the snowflake. The humidity of the incoming airflow is measured in the pipe. The optical observation system consists of a light source, a diffusing sheet

and a high resolution camera. The shadowgraphy of the melting particle allows the characterization of the particle shape and the determination of the time instance at which the particle is fully melted. However, the optical processes cannot detect the amount of liquid water in the particle.

The test matrix for the conducted experiments is given in Tab. 1. The inputs T_a, $\boldsymbol{v}_a$ and RH stand respectively for freestream air temperature, velocity and relative humidity. The snowflake initial temperature is given by T_{p_0}. Uncertainties on the experimental data are given in Tab. 2. The mass m_{drop} is that of the final droplet at the end of the melting process. It is estimated by :

$$m_{\text{drop}} = \frac{\pi}{6}\rho_l d_{\text{drop}}^3 \tag{1}$$

where $\rho_l = 997$ kg.m^{-3} is the density of the liquid water and d_{drop} is the diameter of the final droplet at the end of the melting process. t_m stands for the melting time. The precise definitions of the parameters t_{circ}, $\rho_{p_0}^{\text{bulk}}$, C_{i_0} and $\Phi_{\star_0}$, respectively the time after which the particle appears circular, the bulk density, circularity and sphericity of the initial dry particle (before the melting process has started) will be detailed later in the manuscript.

An estimate of the snowflake initial mass m_{p_0} as a function of m_{drop} is proposed following the methodology described in [5]. It takes into account mass changes due to the particle evaporation and condensation. The main hypothesis is that during the melting process, the mass transfer rate between the particle and the flow is comparable to the evaporation/condensation rate of the liquid droplet after the melting process [5]. This is illustrated in Fig. 3 for the TUDA Run38 test case where the particle projected area during the melting process is plotted. For $t > t_m$, the particle is fully melted and supposed to be spherical. Therefore, under the effect of evaporation/condensation, the square of the diameter of the spherical droplet d^2 follows the so-called d^2-law :

$$\frac{\pi d^2(t)}{4} - \frac{\pi d_{\text{drop}}^2}{4} = K \cdot (t - t_m) \qquad \forall t \geq t_m \tag{2}$$

where K is estimated by the least squares method for $t > t_m$ (see grey dashed line in Fig. 3). Initially valid for $t \geq t_m$, the domain of definition of Eq. (2) is

	Runs	T_a °C	v_a m s^{-1}	RH -	m_{drop} mg	T_{p0} °C	$t_m \approx t_{circ}$ s	$\rho_{p0}^{\mathrm{bulk}}$ kg m^{-3}	C_{i0} -	$\Phi_{\star 0}$ -
Light aggregates	**TUDA Run26**	24.4	0.6	41	1.578	-14.7	8.6	76	0.32	0.93
	TUDA Run27	28.0	0.7	36	1.711	-14.0	6.4	43	0.20	0.88
	TUDA Run28	25.6	0.6	38	1.575	-16.1	7.1	43	0.14	0.92
	TUDA Run36	26.6	0.7	38	0.449	-14.2	2.4	23	0.20	0.69
	TUDA Run37	28.6	0.6	34	2.046	-14.4	5.0	30	0.15	0.76
	TUDA Run38	28.2	0.6	35	0.487	-13.5	3.3	30	0.17	0.77
	TUDA Run39	28.2	0.5	36	1.652	-13.0	4.7	39	0.18	0.85
	TUDA Run40	27.2	0.6	35	1.187	-15.4	3.2	53	0.18	0.77
	TUDA Run51	28.3	0.7	32	1.059	-13.1	4.6	14	0.09	0.78
	TUDA Run71	25.2	0.5	33	2.057	-16.6	5.7	21	0.12	0.92
	TUDA Run72	26.5	0.6	30	0.964	-15.8	3.9	17	0.14	0.82
Dense aggregates	**TUDA Run13**	26.0	0.5	26	1.666	-14.0	11.3	112	0.24	0.91
	TUDA Run25	27.4	0.6	35	2.041	-12.5	8.9	120	0.21	0.86
	IAG Run18	28.4	1.0	6	0.723	-7.0	10.1	145	0.36	0.93
	IAG Run27	33.1	0.9	4	0.318	-4.0	5.6	144	0.35	0.88
	IAG Run38	32.4	0.9	1	0.240	-7.0	7.9	132	0.28	0.98

TABLE 1: Test matrix.

Air temperature (T_a)	± 1 °C
Relative humidity (RH)	± 1.5 %
Air speed (v_a)	± 0.01 m/s
Final droplet mass (m_{drop})	± 3 %

TABLE 2: Experimental data uncertainties.

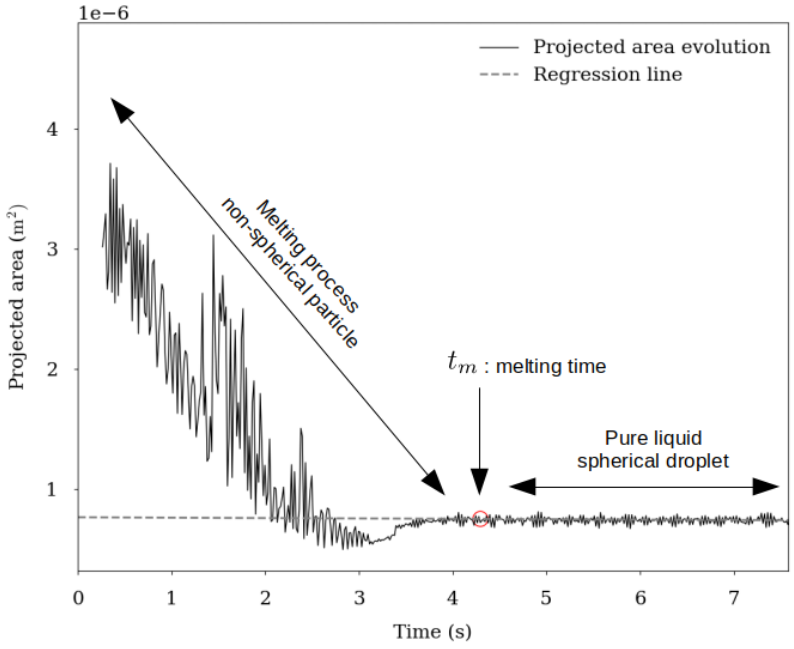

FIGURE 3: Projected area during the melting process (TUDA Run38 test case, see Tab. 1). The red circle stands for the melting time t_m.

Runs	TUDA Run26	TUDA Run27	TUDA Run28	TUDA Run36
$\frac{\Delta m}{m_{p_0}}$	-1.16 %	0.96 %	-2.59 %	1.50 %
Runs	TUDA Run37	TUDA Run38	TUDA Run39	TUDA Run40
$\frac{\Delta m}{m_{p_0}}$	1.64 %	2.74 %	0.57 %	0.33 %
Runs	TUDA Run51	TUDA Run71	TUDA Run72	TUDA Run13
$\frac{\Delta m}{m_{p_0}}$	0.45 %	1.95 %	2.43 %	4.25 %
Runs	TUDA Run25	IAG Run18	IAG Run27	IAG Run38
$\frac{\Delta m}{m_{p_0}}$	0.65 %	25.89 %	8.36 %	25.94 %

TABLE 3: Relative errors $\frac{\Delta m}{m_{p_0}}$ (Eq. (5)).

then extended to $0 \leq t \leq t_m$ in order to calculate d_0 for $t = 0$:

$$d_0 = \sqrt{d_{\text{drop}}^2 - \frac{4K}{\pi} t_m} \tag{3}$$

The snowflake initial mass is then estimated by :

$$m_{p_0} = \frac{\pi}{6} \rho_l d_0^3 \tag{4}$$

The mass variations during the melting process are estimated in Tab. 3 where the relative errors $\frac{\Delta m}{m_{p_0}}$ are defined as :

$$\frac{\Delta m}{m_{p_0}} = \frac{m_{p_0} - m_{\text{drop}}}{m_{p_0}} \tag{5}$$

A positive error stands for mass loss through evaporation while a negative error stands for mass gain by condensation. In agreement with [5], the mass loss is low (1.6 % on average for the absolute value of $\Delta m / m_{p_0}$) for the cases with the highest relative humidity ($RH > 26$ %). In contrast, for the drier cases (IAG Run18, Run27 and Run38), mass losses are higher.

3. Image post-processing for particle characterization

3.1. Particle geometrical model : from 2D image to 3D reconstructed shape

Snowflake features are obtained from the camera (Fig. 2) and a single view of the particle. Thus, volume properties must be reconstructed from this single

image. The procedure used is the one described in [17]. It is briefly reviewed in this section. A grayscale or black and white image of the projected surface of the snowflake is obtained by shadowgraphy. Image post-processing allows the definition of f_{max} and $f_{max}^{\perp}$, respectively the particle maximum and maximum crosswise diameters of Feret (in gray in Fig. 4b). Reconstructed snowflake sha-

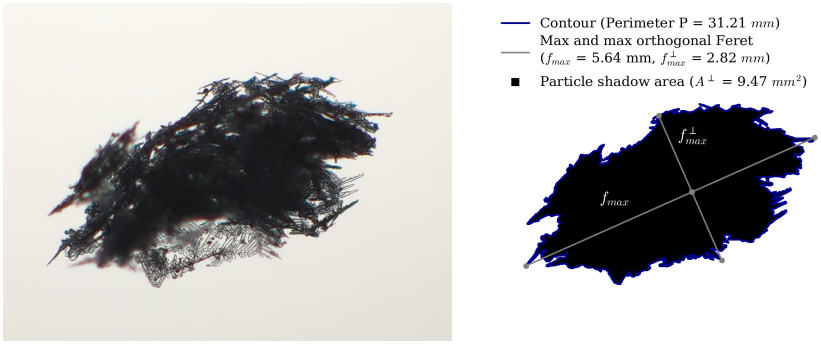

(a) Snowflake grayscale image.

(b) Post processed image.

FIGURE 4: Data post-processing illustration (TUDA Run28 test case, Tab. 1).

dow area $A^{\perp}$ is also derived (in black in Fig. 4b). $f_{max}^{\perp}$ is defined as the largest diameter among all diameters orthogonal to f_{max}. Using Feret's diameters, it can be deduced an ellipse of major semi axis a and minor semi axis c (in gray in Fig. 5) defined by :

$$a = f_{max}/2 \tag{6a}$$

$$c = f_{max}^{\perp}/2 \tag{6b}$$

From the axes of the ellipse it can be constructed either an oblate spheroid (generated by rotation of the ellipse around its z minor axis, Fig. 5a) or a prolate spheroid (generated by rotation of the ellipse around its y major axis, Fig. 5b) of volume $V_\star = \frac{4}{3}\pi a^2 c$ for an oblate spheroid and $V_\star = \frac{4}{3}\pi c^2 a$ for a prolate spheroid. Using these parameters, the following characteristics can be deduced :

$$d_{V_\star} = \left(\frac{6V_\star}{\pi}\right)^{1/3}, \quad \Phi_\star = \frac{\pi d_V^2}{S_\star} \tag{7}$$

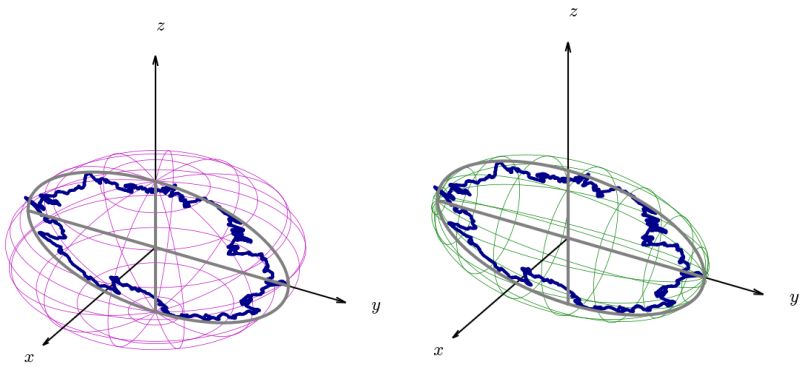

(a) Oblate spheroid reconstruction. (b) Prolate spheroid reconstruction.

FIGURE 5: Oblate and prolate spheroid reconstructions.

where $d_{V_\star}$ is the volume equivalent diameter of the enveloping spheroid and $S_\star$ is the 3D surface of the spheroid given by :

$$S_\star = 2\pi a^2 + \pi \frac{c^2}{e} \ln\left(\frac{1+e}{1-e}\right) \tag{8}$$

for an oblate spheroid and :

$$S_\star = 2\pi a^2 \left(1 + \frac{c}{ae} \arcsin e\right) \tag{9}$$

for a prolate spheroid. $\Phi_\star$ is the spheroid sphericity between 0 and 1. The eccentricity of the spheroid is defined as $e = \sqrt{1 - \frac{c^2}{a^2}}$. It is worth noticing that the sphericity $\Phi_\star$ is different from the real snowflake sphericity Φ. In general we have $\Phi < \Phi_\star \leq 1$. In the same way we have in general $d_V < d_{V_\star}$ with by definition $d_V = (6V/\pi)^{1/3}$, V being the real volume of the snowflake. In the following we will use the terms apparent diameter and apparent sphericity for the parameters $d_{V_\star}$ and $\Phi_\star$ respectively. On the contrary we will speak of the equivalent volume diameter and the real sphericity of the particle to designate the parameters d_V and Φ respectively.

In the following, we will also need to introduce the snowflake circularity. From $A^\perp$ (in black in Fig. 4b), circularity C_i of the 2D projected view of the

particle is defined as :

$$C_i = \frac{4\pi A^{\perp}}{P^2} \tag{10}$$

where P is the perimeter of the projected view (in blue in Fig. 4b).

3.2. Melting time estimation for experiments (t_m)

In order to compare the experimental and numerical results, it is necessary to define t_m, the snowflake melting time [18]. For the experiments, determining t_m is not obvious since it is not possible to accurately identify the time when the last ice residues will disappear by melting. A geometric criterion based on experimentally observable quantities is chosen in this study to define the melting time. t_m is then approximated by t_{sph}, the time when the particle becomes spherical. It is assumed that a spherical particle is almost fully liquid, or at least that it contains a still solid part negligible compared to the liquid part. Particle volume information being not available from the experiments (Sec. 3.1), t_{sph} is evaluated by t_{circ}, the time after which the particle appears circular in the focal plane of the camera, i.e. with a circularity C_i (Eq. (10)) close to 1. Figure 6 shows the time evolution of the reconstructed circularity C_i during the melting process of the snowflake TUDA Run28 (Tab. 1). Each symbol (solid grey circle) stands for a reconstruction of C_i from a 2D view taken at a given time (Eq. (10)). The time evolution of C_i is noisy in time. It can be approximated by the following function C_i^{reg} :

$$C_i^{\text{reg}}(t) = C_{i_0} + (1 - C_{i_0})\, f\left(\frac{t}{t_\infty}\right) \tag{11}$$

where t_∞ is the acquisition time by the camera, C_{i_0} is the initial circularity of the dry snowflake evaluated by Eq. (10), and f is an increasing function of time verifying $f(0) = 0$ and $f(1) = 1$ such that $C_i^{\text{reg}}(0) = C_{i_0}$ and $C_i^{\text{reg}}(t_\infty) = 1$. The function f, defined on $[0; 1]$ is then decomposed as follows :

$$f(t) = h \circ g(t) \tag{12}$$

where h is chosen as the sigmoid function defined by $h(x) = \frac{1}{2} + \frac{1}{2}\tanh(x)$ to be in line with the time evolution profile of C_i (Fig. 6). g is an increasing function

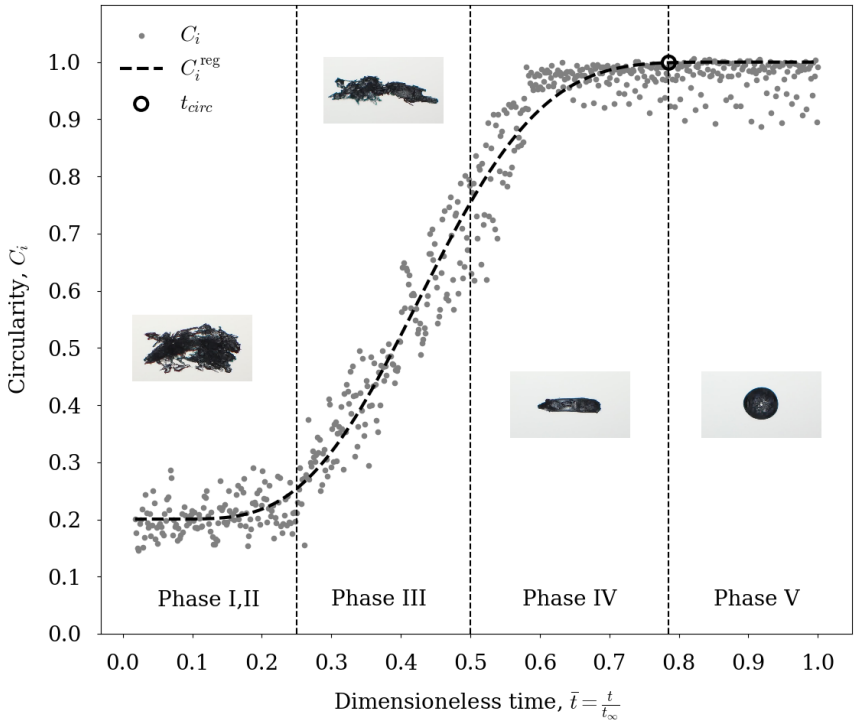

FIGURE 6: Time evolution of the reconstructed circularity C_i during the melting process of the snowflake TUDA Run28 (Tab. 1). Each symbol (solid grey circle) stands for a reconstruction of C_i from a 2D view taken at a given time (Eq. (10)). Best fit curve (dashed black line) is the function C_i^{reg} (Eq. (11)). The empty black circle shows t_{circ} such that $C_i^{\mathrm{reg}}(t_{circ}) = 0.99$.

of time defined on $[0;1]$, with $g(0) = -\infty$ and $g(1) = +\infty$ to span the whole domain of definition of h. The following function g is chosen :

$$g(t) = \kappa_1 \left[\frac{1}{1-t^{\kappa_2}} - \frac{1}{t^{\kappa_2}} \right] \tag{13}$$

The values $\kappa_1 = 0.78$ and $\kappa_2 = 0.83$ are selected as minimizing the least square error between $C_i^{\text{reg}}(t)$ and $C_i(t)$.

By convention t_{circ}, and thus t_m, will be defined as $C_i^{\text{reg}}(t_{circ}) = 0.99$. In the rest of the manuscript, t_{circ} will be chosen as the melting time t_m. The values of t_{melt} for each snowflake are summarized in Tab. 1.

3.3. Snowflake bulk density time evolution from experiments

The time evolution of the bulk density is estimated by :

$$\rho_p^{\text{bulk}}(t) = \frac{m_p(t)}{V_\star(t)} \tag{14}$$

where, at each instant, $m_p(t)$ is the mass of the snowflake and $V_\star(t)$ is the volume of the reconstructed oblate spheroid from planar images of the particle (Sec. 3.1). The choice of an oblate and not prolate spheroid is the same as the one motivated in Mitra's model [16]. The initial value of $\rho_p^{\text{bulk}}(t)$, denoted $\rho_{p_0}^{\text{bulk}}$, is presented in Tab. 1. It stands for the bulk density of the dry snowflake before the melting process has started.

During the melting process, the mass $m_p(t)$ of the particle is between m_{p_0} and m_{drop}. For each case in Tab. 1, the ratio $(\Delta m/m_{p_0}) \,/\, \left(\Delta\rho/\rho_{p_0}^{\text{bulk}}\right)$ is less than 3.9 %, where $\Delta m/m_{p_0}$ is defined in Eq. (5) and $\Delta\rho/\rho_{p_0}^{\text{bulk}} = \left(\rho_{p_0}^{\text{bulk}} - \rho_l\right)/\rho_{p_0}^{\text{bulk}}$. Thus, throughout the melting process, the contribution of the particle mass variation $(\Delta m/m_{p_0})$ to the bulk density variation $(\Delta\rho/\rho_{p_0}^{\text{bulk}})$ is negligible compared to that of the particle volume variation. Therefore, a constant value for $m_p(t)$ is chosen in Eq. (14) to estimate the bulk density $\rho_p^{\text{bulk}}(t)$ from experiments. This constant is chosen equal to m_{drop}, the mass of the drop at the end of the melting process, m_{drop} being a priori estimated more accurately than m_{p_0}.

In the rest of the manuscript, a dimensionless value of $\rho_p^{\text{bulk}}(t)$, noted $\bar{\rho}_p^{\text{bulk}}(t)$, is used :

$$\bar{\rho}_p^{\text{bulk}}(t) = \frac{\rho_p^{\text{bulk}}(t) - \rho_{p_0}^{\text{bulk}}}{\rho_l - \rho_{p_0}^{\text{bulk}}} \tag{15}$$

where $\rho_l = 997$ kg.m^{-3} is the density of the liquid water which is also the final value of the bulk density. $\bar{\rho}_p^{\text{bulk}}(t)$ lies thus between 0 for the initial dry particle and 1 for the final liquid droplet at the end of the melting process.

Figure 7 shows the time evolution of $\bar{\rho}_p^{\text{bulk}}$ (black symbols) for the test case TUDA - Run28 (Tab. 1). Time is scaled by the experimental melting time t_m

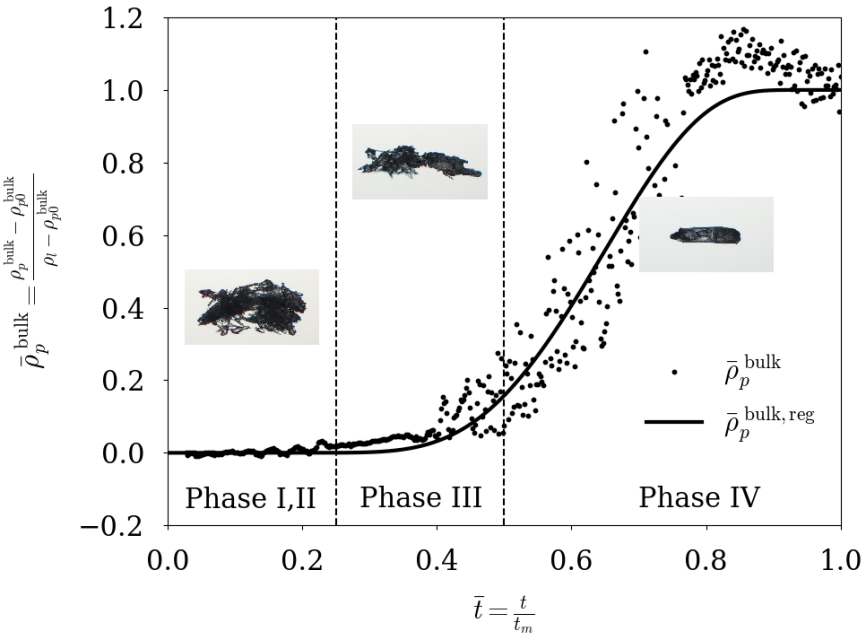

FIGURE 7: Time evolution of $\bar{\rho}_p^{\text{bulk}}$ and $\bar{\rho}_p^{\text{bulk,reg}}$. TUDA - Run28 test case (Tab. 1).

(Sec. 3.2). For the sake of completeness, Figs. A.16, A.17 and A.18 show the time evolutions $\bar{\rho}_p^{\text{bulk}}(t)$ (black symbols) for all the test cases of Tab. 1. The results in Fig. 7 are representative of all test cases, which allows us to use it as a baseline for conducting the analysis in this paragraph. In some cases, $\bar{\rho}_p^{\text{bulk}}(t) > 1$ for stage IV (Fig. 1), at a time when the melting process leads to privileged directions for the particle before the final collapse of the snowflake structure. Thus, for stage IV, the reconstructed spheroid and therefore the value of $\rho_p^{\text{bulk}}(t)$ depend strongly on the orientation of the particle on the image used to make the geometric 2D-to-3D reconstruction. This leads to a strong dispersion

of the results with sometimes a reconstructed $\rho_p^{\text{bulk}}(t)$ higher than 1 when the particle is highly anisotropic (needle shape for example).

For the majority of cases (Figs. A.16 and A.17), $\bar{\rho}_p^{\text{bulk}}(t)$ shows three branches, as well as the time evolution of the circularity $C_i(t)$ (Fig. 6). Each of these branches can be related to the stages of Mitra's description (Fig. 1) :

— At early times ($t/t_m < 0.25$, first branch), the evolution is slow. This corresponds to stages I and II described in [16] and summarized in Fig. 1. Melting is most intense at the periphery of the snowflake. Capillary forces lead to the drainage of the liquid water from the periphery of the particle towards its center, without damaging the main ice frame. The main structure of the snowflake being preserved, the change in the bulk density is limited.

— At intermediate times ($0.25 < t/t_m < 0.8$, second branch), the evolution is steeper. This corresponds to the stage III and the beginning of stage IV in [16] and Fig. 1, with the collapse of the snowflake structure on itself and a sharp increase in the bulk density.

— At late times ($t/t_m > 0.8$, third branch), the evolution is slow again. This corresponds to the end of stage IV in [16] and Fig. 1. The particle is quasi-spherical and mainly composed of liquid water. Its density is almost equal to ρ_l, and $\bar{\rho}_p^{\text{bulk}}(t) \approx 1$.

In agreement with the three branches for the time evolution of the bulk density, a sigmoid-type function is used to approximate $\bar{\rho}_p^{\text{bulk}}(t)$. In Fig. 7 (and in Figs. A.16 and A.17), the black solid line shows the sigmoid functions as regression curves (best fit) among the dispersed reconstructed values of $\bar{\rho}_p^{\text{bulk}}(t)$ from the experiments. The regression curves (black solid lines), noted $\bar{\rho}_p^{\text{bulk,reg}}$, will be used as experimental references to evaluate the different models proposed for $\rho_p^{\text{bulk}}(t)$ (Sec. 4).

For the three IAG cases and TUDA Run13 and Run25 cases (Fig. A.18), branch 1 of the sigmoid does not exist. For these five configurations (Tab. 1), the initial density of the dry snowflake $\rho_{p_0}^{\text{bulk}}$ is higher than $100\,\text{kg}\,\text{m}^{-3}$ (dense aggregates), while it is lower than $100\,\text{kg}\,\text{m}^{-3}$ for the other test cases (light ag-

gregates). For light aggregates, stages I and II of the sequence described by Mitra (Fig. 1) correspond to the melting of peripheral structure, which slightly alter the particle bulk volume, leading to an almost constant value for $\bar{\rho}_p^{\text{bulk}}(t)$ during the early times (branch 1 in Fig. 7). On the other hand, for dense aggregates, the melting process starts directly at stage III (Fig. 1) with a predominant melting in the core of the particle, leading to a more significant decrease in the bulk volume and an increase in the bulk density. Thus, although the sigmoid-type regression was proposed for the case of light snowflakes for which the function $\bar{\rho}_p^{\text{bulk}}(t)$ has 3 branches, Fig. A.18 shows that it is also suitable for cases of dense snowflakes for which the first branch is absent.

Figure 8 shows the mass probability distribution of natural snowflakes as a function of their dry bulk density $\rho_{p_0}^{\text{bulk}}$ (blue histograms) and allows estimating the occurrence probabilities (in mass) between light and dense aggregates. The black solid line stands for the associated cumulative distribution function

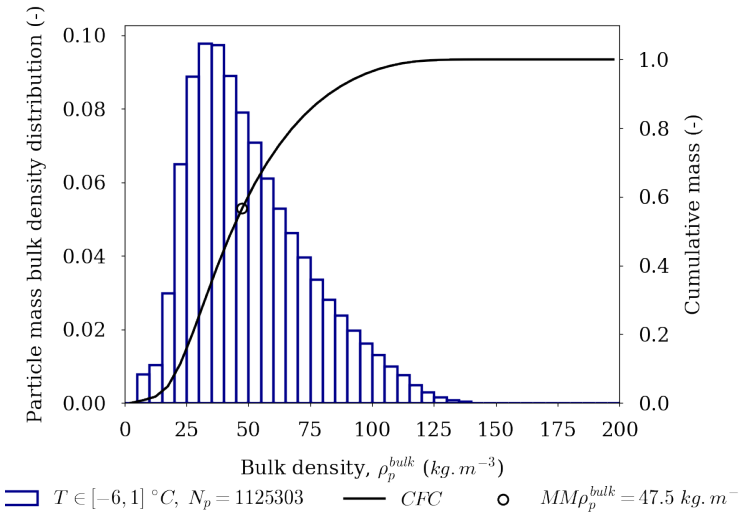

FIGURE 8: Blue histograms : mass probability distribution of natural snowflakes as a function of their dry bulk density $\rho_{p_0}^{\text{bulk}}$. Solid line : associated cumulative distribution function. Black circle : mass median value.

between 0 and 1. The distribution was measured during a flight test in the fra-

mework of the European project ICEGENESIS [19]. Five flights were performed from Dijon, France to fly over an area around the regional airport Les Éplatures located in La Chaux-de-Fonds, Switzerland. Particle images necessary for the 2D-to-3D geometric reconstruction of the oblate or prolate spheroid (Sec. 3.1) were recorded by a PIP probe aboard the SAFIRE ATR42-300 research aircraft. Figure 8 illustrates flight F210007 of January 28, 2021 which is representative of all flights. During this flight at an altitude between 1000 m and 2000 m, the typical size of the recorded particles is 1 to 3 mm, which is in agreement with of snow aggregates. The black circle in Fig. 8 is the mass median value equal to around 47.5 kg.m^{-3}, the mass of each particle being estimated by a mass/diameter relationship [20]. Aggregates of density greater than 100 kg.m^{-3} represent less than 2% of the total snowflake mass, which allows to confirm that the majority of the snowflakes are light aggregates according to our classification (i.e. $\rho_{p_0}^{\text{bulk}} < 100$ kg.m^{-3} for light aggregates).

4. Melting models for snowflakes

During the melting step, the whole snowflake is assumed to be in thermal equilibrium and at the melting temperature ($T_0 = 273.15\,\text{K}$). The liquid water is assumed to cover the ice core so that there is no sublimation but only evaporation.

The evolution of the particle during the melting process can be fully characterized by three geometric parameters : its liquid fraction Y_l, its diameter d_{ref} (d_V or $d_{V_\star}$ depending on whether we use a type I or a type II geometric model) and its sphericity Φ_{ref} (apparent or real depending on whether we use a type I or a type II geometric model). Writing the conservation of energy and mass we obtain the following two equations :

$$L_f \cdot \frac{d}{dt}\left(Y_l \cdot m_p\right) = \pi d_{ref} \cdot \frac{Nu\left(d_{ref}, \Phi_{ref}\right)}{\Phi_{ref}} \cdot k_a \cdot \left(T_a - T_0\right) - \dot{m}_{ev} L_s \tag{16a}$$

$$\frac{d}{dt}(m_p) = -\dot{m}_{ev} \tag{16b}$$

with

$$\dot{m}_{ev} = \pi \rho_a d_{ref} \cdot \frac{Sh\left(d_{ref}, \Phi_{ref}\right)}{\Phi_{ref}} \cdot D_{v,a} \cdot \left(Y_{v,0} - Y_{v,\infty}\right) \tag{17}$$

where $\dot{m}_{ev}$ is the evaporation rate. Equation (16a) describes the heat exchange that drives the melting process while Eq. (16b) stands for the particle mass loss due to the evaporation rate itself defined by Eq. (17). d_{ref} and Φ_{ref} are respectively the particle reference diameter and sphericity. The parameters ρ_a, T_a and k_a are respectively the freestream density, temperature and thermal conductivity. $D_{v,a}$ is the diffusion coefficient of steam in dry air. Nu and Sh are respectively the Nusselt and Sherwood numbers which depend on d_{ref} and Φ_{ref}. The coefficients L_s and L_f are respectively the latent heats of sublimation and melting. $Y_{v,\infty}$ is the freestream steam mass fraction while $Y_{v,0}$ is the steam mass fraction in the saturated region above the particle. $Y_{v,0}$ is a known parameter, being a function of T_0 and the freestream pressure P_∞.

Eqs. (16) can be solved by an explicit numerical method. The finite difference numerical scheme is the following :

$$L_f(T_0) \cdot \frac{\left(Y_l \cdot m_p\right)^{n+1} - \left(Y_l \cdot m_p\right)^n}{\Delta t} = \pi d_{ref}^n \cdot \frac{Nu^n}{\Phi_{ref}^n} \cdot k_a \cdot \left(T_a - T_0\right) - \dot{m}_{ev}^n L_s(T_0) \tag{18a}$$

$$\frac{m_p^{n+1} - m_p^n}{\Delta t} = -\dot{m}_{ev}^n \tag{18b}$$

with

$$\dot{m}_{ev}^n = \pi \rho_a d_{ref}^n \cdot \frac{Sh^n}{\Phi_{ref}^n} \cdot D_{v,a} \cdot \left(Y_{v,0} - Y_{v,\infty}\right) \tag{19a}$$

$$d_{ref}^n = \left(\frac{6 m_p^n}{\pi \rho_{p_{ref}}^n} \right)^{1/3} \tag{19b}$$

where Δt is the time step defined as $\Delta t = 0.001 \cdot \min(\tau_{melt}, \tau_{evap})$, τ_{melt} and τ_{evap} being respectively the melting and evaporative characteristic time scales. Superscripts $\cdot^n$ and $\cdot^{n+1}$ denote respectively the variables estimated at times t^n and t^{n+1}.

By definition one has $m_p = \rho_{p_{ref}} \pi d_{ref}^3 / 6$, where $\rho_{p_{ref}}$ corresponds to the particle core density or to the particle bulk density depending on the type of

geometric model chosen. If the expressions of Nu and Sh are assumed to be known, there remain 4 unknowns m_p, Y_l, $\rho_{p_{ref}}$, and Φ_{ref} for only two differential equations (Eqs. (16)). It is therefore necessary to provide two additional closure laws. This is done in the following by relating $\rho_{p_{ref}}$ and Φ_{ref} to Y_l.

4.1. Mitra's model [16]

Based on an analogy between the electrostatic and diffusion problems for the definition of the evaporative flux, and the hypothesis $Nu = Sh$ assuming comparable thermal and mass diffusivities, Eqs. (16) can be rewritten as (Mitra [16]) :

$$L_f(T_0) \cdot \frac{d}{dt}(Y_l \cdot m_p) = 4\pi f_v C k_a \left(T_a - T_0\right) - \dot{m}_{ev} L_s(T_0) \tag{20a}$$

$$\frac{d}{dt}(m_p) = -\dot{m}_{ev} \tag{20b}$$

$$\dot{m}_{ev} = 4\pi f_v C \rho_a D_{v,a} L_s(T_0) \left(Y_{v,0} - Y_{v,\infty}\right) \tag{20c}$$

where C is defined as a capacitance and has the dimension of a length. For instance, for a sphere of diameter d, the capacitance is simply given by $C = d/2$. Convective effects are accounted for by the mean ventilation coefficient f_v which stands for the ratio between the mass flow rate of a moving particle and that of a stationary particle (pure diffusion) [21]. f_v is analogous to the Sherwood number Sh, and $Sh = 2f_v$ is verified for a sphere. The analogy between the terms of Eqs. (16) and (20) is summarized in Tab. 4. Thus, defining d_{ref}, Φ_{ref},

Term in Eq. (16)	Term in Eq. (20)
d_{ref}	$2C$
$\frac{Sh}{\Phi_{ref}}$	$2f_v$

TABLE 4: Analogy of terms between Eqs. (16) and (20).

Nu and Sh in the general system of Eqs. (16) is equivalent to defining C, f_v and d_{ref} in the system of Mitra Eqs. (20). The reference diameter d_{ref}, noted

a_i in the original paper of Mitra [16], is given by :

$$d_{ref}(Y_l) \equiv a_i(Y_l) = \left(\frac{3m_p}{4\pi \cdot AR(Y_l) \cdot \rho_p^{\text{Mitra}}(Y_l)} \right)^{1/3} \tag{21}$$

where AR is the ratio between the radii of the major and minor axes of the melting snowflake, assuming the particle may be approximated by an oblate spheroid. ρ_p^{Mitra} is the snowflake density (see below). Thus, the dataset (C, f_v, AR, ρ_p^{Mitra}) can be equivalently defined instead of (C, f_v, d_{ref}) at each stage of the melting process. To do this, Mitra suggests that these parameters depend only on the particle liquid mass fraction Y_l, leading to the following definitions :

$$AR\,(Y_l) = 0.3 + 0.7 \cdot Y_l \tag{22a}$$

$$\rho_p^{\text{Mitra}}\,(Y_l) = 20 + 980 \cdot Y_l \tag{22b}$$

$$\frac{C}{C_\star} = 0.8 + 0.2 \cdot Y_l \tag{22c}$$

where $C_\star$ is the capacitance of a simple oblate spheroid. Both $C_\star$ and f_v are functions of AR, ρ_p^{Mitra} and m_p which themselves depend on Y_l [16]. One major drawback of Eqs. (22), is that $AR(0) = 0.3$ and $\rho_p^{\text{Mitra}}(0) = 20$ kg.m^{-3} for the initial dry snowflake ($Y_l = 0$) regardless of its shape. No information on the geometric characterization of the initial dry particle is taken into account, considering in the same way a dense ice crystal and an aggregated light snowflake. Another weakness of the model is that it assumes a linear evolution of the particle bulk density with respect to the liquid fraction.

In the rest of the manuscript, Mitra's model will simply be noted as *Mitra's*.

4.2. Ice core density based approach : from ice crystals to snowflakes

This approach was initially developed for ice crystal icing [22] where ice crystals are assumed to be rather compact with a bulk density of the same order as the ice core density $\rho_s = 917$ kg.m^{-3}. Consistently with [17], the initial density ρ_{p_0} of the dry snowflake (i.e. before the melting process has started), can be written :

$$\rho_{p_0} = \rho_{p_0}^{\text{core}} = \rho_s \tag{23}$$

During the melting process, the snowflake of initial density $\rho_{p_0}^{\text{core}}$ will turn into a spherical liquid droplet of density $\rho_l = 997$ kg.m^{-3}. For the ice core density based model, the internal porosity is assumed to be negligible. This allows writting for the evolution of the snowflake density ρ_p^{core} during the melting process :

$$\rho_p^{\text{core}}(Y_l) = \left(\frac{Y_l}{\rho_l} + \frac{1 - Y_l}{\rho_{p_0}^{\text{core}}} \right)^{-1} \tag{24}$$

The reference diameter d_{ref} is defined as the volume equivalent diameter, hence we have : $d_{ref} = d_V$. By definition of the core density, we also have :

$$d_V = \left(\frac{6 m_p}{\pi \rho_p^{\text{core}}(Y_l)} \right)^{1/3} \tag{25}$$

where $\rho_p^{\text{core}}(Y_l)$ is given by Eq. (24) and the evolution of m_p is driven by the evaporation law (Eq. (17)).

The Nusselt and Sherwood correlations are those in [12]. They are based on a generalization of the Frossling correlation [13] and can be written as :

$$Nu(\Phi, Re_p) = 2\sqrt{\Phi} + 0.55 Pr^{1/3} \Phi^{1/4} \sqrt{Re_p} \tag{26a}$$

$$Sh(\Phi, Re_p) = 2\sqrt{\Phi} + 0.55 Sc^{1/3} \Phi^{1/4} \sqrt{Re_p} \tag{26b}$$

where Pr and Sc are respectively the Prandtl and Schmidt numbers and Φ the particle sphericity. The particle Reynolds number Re_p is defined as :

$$Re_p = \frac{\rho_a d_{ref} ||\boldsymbol{u}_p - \boldsymbol{u}_a||}{\mu_a} \tag{27}$$

where $\boldsymbol{u}_p$ is the particle velocity, $d_{ref} = d_V$ (Eq. (25)), and ρ_a, μ_a and $\boldsymbol{u}_a$ are respectively the air density, dynamic viscosity and velocity. A linear evolution of Φ versus Y_l is assumed, between Φ_0 (sphericity of the initial dry snowflake) and 1 (liquid droplet at the end of the melting) :

$$\Phi(Y_l) = (1 - Y_l) \cdot \Phi_0 + Y_l \tag{28}$$

In this study, the initial sphericity Φ_0 being not known a priori, it is estimated from the image of the dry snowflake (Fig. 4) by $\Phi_0 = C_{i_0}$ (Eq. (10)), C_{i_0} being the initial circularity of the dry snowflake.

In the rest of the manuscript, the ice core density based model will simply be noted as ρ_p^{core} model.

4.3. A new ice bulk density based model

4.3.1. Generalities

The reference diameter d_{ref} is defined as the apparent diameter of the snowflake $d_{V_\star}$:

$$d_{ref} = d_{V_\star} = \left(\frac{6V_\star}{\pi}\right)^{1/3} = \left(\frac{6m_p}{\pi\rho_p^{\text{bulk}}(Y_l)}\right)^{1/3} \tag{29}$$

where $V_\star$ is the volume of the reconstructed spheroid from planar images of the particle (Eq. (7), Sec. 3.1).

The correlations for Nu and Sh are those in Eqs. (26) where the characteristic length in the definition of the particle Reynolds number Re_p is $d_{V_\star}$, and the sphericity Φ_{ref} is that of the reconstructed spheroid $\Phi_\star$. It is worth noticing that contrary to the real sphericity Φ, $\Phi_\star$ does not change too much during the melting process. As can be seen in Tab. 1, the initial apparent sphericity $\Phi_{\star_0}$ is always close to 0.9. Hence arbitrarily postulating the linear model :

$$\Phi_\star(Y_l) = (1 - Y_l)\,\Phi_{\star_0} + Y_l \tag{30}$$

will not strongly affect the global accuracy of the melting model.

4.3.2. Model calibration

The objective here is to propose a law for $\rho_p^{\text{bulk}}(Y_l)$ which, combined with the law in Eq. (30) for $\Phi_\star$ will allow to complete the model in Eqs. (16). As seen before, we can introduce a dimensionless expression of ρ_p^{bulk}, denoted $\bar{\rho}_p^{\text{bulk}}$, defined as :

$$\bar{\rho}_p^{\text{bulk}}(Y_l) = \frac{\rho_p^{\text{bulk}}(Y_l) - \rho_{p_0}^{\text{bulk}}}{\rho_l - \rho_{p_0}^{\text{bulk}}} \tag{31}$$

where $\rho_l = 997$ kg.m^{-3} and $\rho_{p_0}^{\text{bulk}} = \rho_p^{\text{bulk}}(0)$ is the bulk density of the initial dry snowflake. Thus, defining $\rho_p^{\text{bulk}}(Y_l)$ is similar to defining both a model $\bar{\rho}_p^{\text{bulk}}(Y_l)$ and $\rho_{p_0}^{\text{bulk}}$.

To derive a model for $\bar{\rho}_p^{\text{bulk}}(Y_l)$, time evolutions $\bar{\rho}_p^{\text{bulk}}(t)$ obtained from experimental observations (Sec. 3.3), and then denoted by $\bar{\rho}_p^{\text{bulk,exp}}(t)$ can be used. However, since Y_l is not an experimentally measured quantity, we cannot find

the $\bar{\rho}_p^{\text{bulk}}(Y_l)$ function only from the experimental data. To do so, one must combine modeling and experimental results and solve an inverse problem. Since the liquid mass fraction Y_l is a monotonic function of time, a sigmoid shape is also assumed for $\bar{\rho}_p^{\text{bulk}}(Y_l)$ in coherence with the sigmoid shape functions used for $\bar{\rho}_p^{\text{bulk,exp}}(t)$ (Sec. 3.3 and Figs. A.16, A.17 and A.18). This leads to the following model for $\bar{\rho}_p^{\text{bulk}}(Y_l)$:

$$\bar{\rho}_p^{\text{bulk}}(Y_l) = \frac{1}{2} + \frac{1}{2}\tanh\left(\frac{c_1}{1-Y_l^{c_2}} - \frac{c_1}{Y_l^{c_2}}\right) \tag{32}$$

where c_1 and c_2 are positive constants to be determined. By construction Eq. (32) verifies the boundary conditions $\bar{\rho}_p^{\text{bulk}}(Y_l) \underset{Y_l \to 0}{\longrightarrow} 0$ and $\bar{\rho}_p^{\text{bulk}}(Y_l) \underset{Y_l \to 1}{\longrightarrow} 1$.

To find the values of the constants c_1 and c_2, we proceeded in two steps. Firstly, for each of the runs (i) of the experimental database (Tab. 1), we identified the optimal pair $(c_{1,\text{best}}^{(i)}, c_{2,\text{best}}^{(i)})$ that minimizes the following cost function :

$$err(c_1, c_2) = \frac{1}{t_m}\int_0^{t_m} \left[\bar{\rho}_p^{\text{bulk}}(Y_l(t)) - \bar{\rho}_p^{\text{bulk,reg}}(t)\right]^2 dt \tag{33}$$

where $\bar{\rho}_p^{\text{bulk}}(Y_l(t))$ is computed by numerically solving the model of Eqs. (16) closed with Eqs. (30) and (32). Next, we correlated the values of $(c_{1,\text{best}}^{(i)}, c_{2,\text{best}}^{(i)})$ with the values of the bulk density $\rho_{p_0}^{\text{bulk}}$ and circularity C_{i_0} of the particles at the initial time. We will now detail these two steps. Figure 9 shows the result of the optimization process where $\bar{\rho}_p^{\text{bulk}}(Y_l(t))$ (magenta solid line) and $\bar{\rho}_p^{\text{bulk,reg}}(t)$ (black dashed line) are compared for the test case TUDA - Run28 (Tab. 1). For this particular case, the optimized values for c_1 and c_2 are respectively $c_{1,\text{best}} = 0.72$ and $c_{2,\text{best}} = 0.54$. See Tab. 5 for the values of $c_{1,\text{best}}$ and $c_{2,\text{best}}$ for all cases in Tab. 1.

It can be seen that the values of $c_{1,\text{best}}^{(i)}$ and $c_{2,\text{best}}^{(i)}$ can vary significantly from one run (i) to another. They can therefore not simply be assumed to be constant. For the model to be closed, it is necessary to be able to express these two parameters in terms of the geometric parameters used to characterize the shape of the snowflake. A first simple solution consists in relying on the value of the bulk density at the initial time. This model will be called *model P1* in the following. Another solution, a little more complex but presumably more

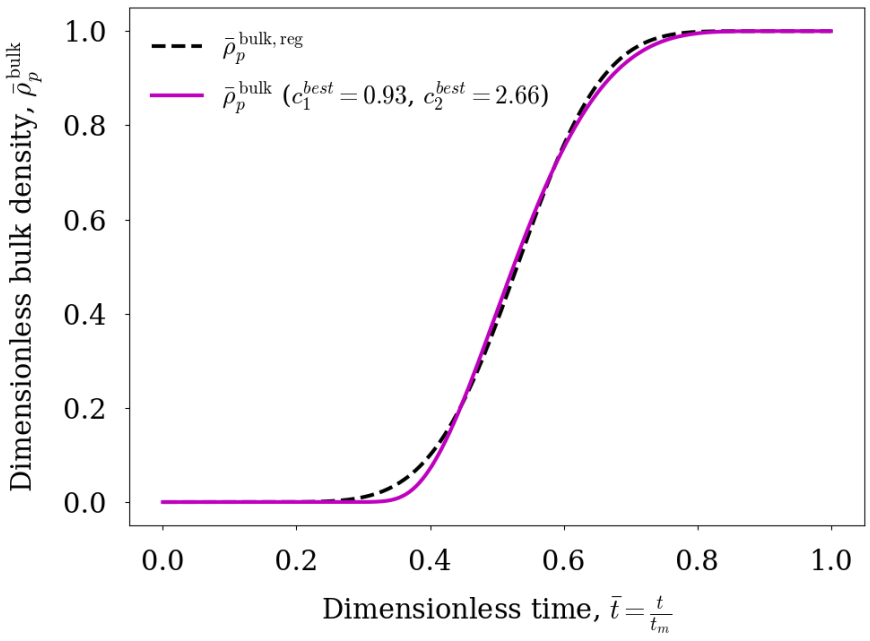

FIGURE 9: Comparison between $\bar{\rho}_p^{\text{bulk}}(Y_l(t))$ and $\bar{\rho}_p^{\text{bulk,reg}}(t)$ at the end of the optimization process of c_1 and c_2 for the TUDA - Run28 test case (Tab. 1).

Runs	$\boldsymbol{c_{1,\text{best}}}$	$\boldsymbol{c_{2,\text{best}}}$
TUDA Run13	0.40	0.51
TUDA Run25	0.72	0.54
TUDA Run26	0.40	1.93
TUDA Run27	0.50	2.10
TUDA - Run28	0.81	2.61
TUDA - Run36	0.71	6.57
TUDA - Run37	0.62	2.24
TUDA - Run38	0.75	3.21
TUDA - Run39	0.56	2.63
TUDA - Run40	0.94	1.84
TUDA - Run51	0.44	2.54
TUDA - Run71	0.72	3.52
TUDA - Run72	0.83	4.55
IAG - Run18	0.40	1.02
IAG - Run27	0.40	1.05
IAG - Run38	0.40	1.05

TABLE 5: Best coefficients $c_{1,\text{best}}$ and $c_{2,\text{best}}$ (Eq. (32)) minimizing the L_2-norm between $\bar{\rho}_p^{\text{bulk}}(Y_l(t))$ and $\bar{\rho}_p^{\text{bulk,reg}}(t)$ (Eq. (33)).

accurate, consists in making c_1 and c_2 dependent on both $\rho_{p_0}^{\text{bulk}}$ and the initial circularity C_{i_0}. This model will be called *model P2* in the following. c_1 and c_2 can be seen as the two parameters that control on the one hand the value of $Y_l^{\#}$ for which $\bar{\rho}_p^{\text{bulk}}$ is 0.5, and on the other hand the value of the derivative of $\bar{\rho}_p^{\text{bulk}}$ in $Y_l^{\#}$. However, according to the experimental results, it has been seen that for a light snowflake, stage I of the Mitra's description [16] (Fig. 1) during which the snowflake melts (thus Y_l increases) at almost constant apparent volume (thus at constant $\bar{\rho}_p^{\text{bulk}}$) is much longer than for a dense snowflake. It is therefore reasonable to think that there is a good correlation between $\bar{\rho}_{p_0}^{\text{bulk}}$ and (c_1, c_2). But, if $\bar{\rho}_{p_0}^{\text{bulk}}$ is not the only explanatory variable, taking into account the initial circularity C_{i_0} of the snowflake can only improve the accuracy of the model, with the risk of a greater dependence on the experimental database used for the identification of the parameters of the law. In the rest of the manuscript, for the sake of simplicity, $c_{1,\text{best}}$ and $c_{2,\text{best}}$ will be noted simply as c_{11} and c_{21} for *model P1*, and c_{12} and c_{22} for *model P2*.

As will be confirmed a posteriori (Figs. 10 and 11), there is a pretty good linear dependency between the logarithms of c_{11}, c_{21} and $\frac{\rho_{p_0}^{\text{bulk}}}{\rho_s}$ on the one hand for *model P1*, and between the logarithms of c_{12}, c_{22}, C_{i_0} and $\frac{\rho_{p_0}^{\text{bulk}}}{\rho_s}$ on the other hand for *model P2*. Thus, the following log-linear relations are proposed for *model P1* :

$$\ln(c_{21}) = A_{11} \ln\left(\frac{\rho_{p_0}^{\text{bulk}}}{\rho_s}\right) + B_{11} \tag{34a}$$

$$\ln(c_{11}^{\alpha_1} c_{21}) = A_{12} \ln\left(\frac{\rho_{p_0}^{\text{bulk}}}{\rho_s}\right) + B_{12} \tag{34b}$$

and for *model P2* :

$$\ln(c_{22}) = A_{21} \ln\left(\frac{\rho_{p_0}^{\text{bulk}}}{\rho_s} \cdot C_{i_0}^{\beta_2}\right) + B_{21} \tag{35a}$$

$$\ln(c_{12}^{\alpha_2} c_{22}) = A_{22} \ln\left(\frac{\rho_{p_0}^{\text{bulk}}}{\rho_s} C_{i_0}^{\gamma_2}\right) + B_{22} \tag{35b}$$

where the set of coefficients (A_{11}, B_{11}) (resp. (A_{12}, B_{12}), (A_{21}, B_{21}) and (A_{22}, B_{22})) is obtained by a linear regression between the two logarithmic terms in Eq. (34a)

(resp. Eq. (34b), Eq. (35a) and Eq. (35b)). The parameters α_1, β_2 (respectively in Eq. (34b) and (35a)), and the set of parameters (α_2, γ_2) in Eq. (35b) are chosen to minimize $1 - R^2$ via an optimization procedure, where R^2 is the coefficient of determination of the linear regression in question. The results of the linear regression for each of Eqs. (34a), (34b), (35a) and (35b) are :

$$A_{11} = -0.686 \quad , B_{11} = -1.475 \quad , R^2 = 0.76 \tag{36a}$$

$$A_{12} = -0.799 \quad , B_{12} = -1.908 \quad , R^2 = 0.77 \tag{36b}$$

$$A_{21} = -1.113 \quad , B_{21} = -0.927 \quad , R^2 = 0.87 \tag{36c}$$

$$A_{22} = -1.070 \quad , B_{22} = -0.646 \quad , R^2 = 0.88 \tag{36d}$$

with the following values for α_1, α_2, β_2 and γ_2 :

$$\alpha_1 = 0.344\,,\ \alpha_2 = -0.201\,,\ \beta_2 = -0.978\,,\ \gamma_2 = -1.073 \tag{37}$$

Figures 10 and 11 show the linear regressions obtained from Eqs. (34) and (35) respectively (solid lines). Symbols represent each of the test cases in Tab. 1.

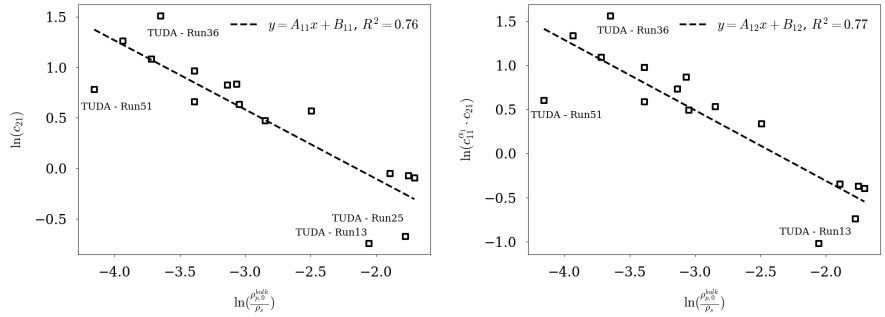

(a) *model P1* (Eq. (34a)) (b) *model P1* (Eq. (34b))

FIGURE 10: Optimal linear regressions (i.e. minimizing $1 - R^2$) obtained from Eqs. (34) (*model P1*).

The R^2 factors are closer to 1 for *model P2* (Eqs. (36c) and (36d)) than for *model P1* (Eqs. (36a) and (36b)), confirming that the proposed linear regression is more accurate when an additional geometric parameter, namely C_{i_0} here,

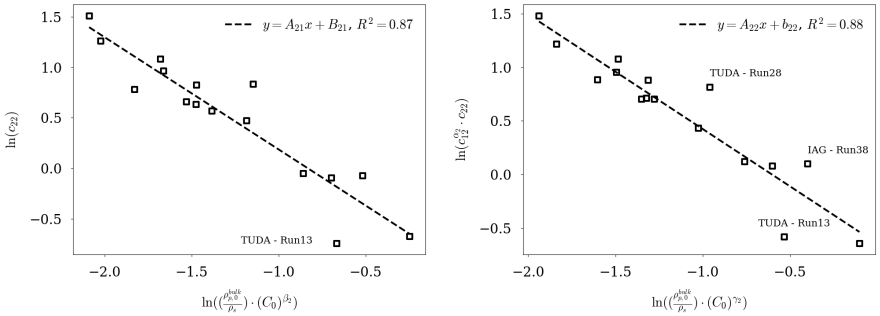

(a) *model P2* (Eq. (35a)) (b) *model P2* (Eq. (35b))

FIGURE 11: Optimal linear regressions (i.e. minimizing $1-R^2$) obtained from Eqs. (35) (*model P2*).

is available. However, *model P1* remains acceptable for estimating the optimal coefficients c_1 and c_2 as a function of ρ_{p0}^{bulk} only. Finally, from Eqs. (34) and (35), the coefficients c_{11}, c_{21}, c_{12} and c_{22} are simply given by :

$$c_{21} = E_{21}\left(\frac{\rho_{p0}^{\text{bulk}}}{\rho_s}\right)^{F_{21}} \tag{38a}$$

$$c_{11} = E_{11}\left(\frac{\rho_{p0}^{\text{bulk}}}{\rho_s}\right)^{F_{11}} \tag{38b}$$

for the *model P1* and :

$$c_{22} = E_{22}\left(\frac{\rho_{p0}^{\text{bulk}}}{\rho_s}\cdot C_{i_0}^{G_{22}}\right)^{F_{22}} \tag{39a}$$

$$c_{12} = E_{12}\left(\frac{\rho_{p0}^{\text{bulk}}}{\rho_s}\cdot C_{i_0}^{G_{12}}\right)^{F_{12}} \tag{39b}$$

for the *model P2*. The coefficients of Eqs. (38) and (39) are given in Tab. 6.

E_{11}	E_{12}	E_{21}	E_{22}	F_{11}	F_{12}	F_{21}	F_{22}	G_{12}	G_{22}
0.285	0.246	0.229	0.396	-0.329	-0.215	-0.686	-1.113	1.363	-0.978

TABLE 6: Coefficients of Eqs. (38) and (39).

Figure 12 compares the evolution of $\bar{\rho}_p^{\text{bulk,exp}}(t)$ and $\bar{\rho}_p^{\text{bulk}}(Y_l(t))$ for a light

aggregate (Fig. 12a, corresponding to TUDA-Run27 in Tab. 1) and a dense aggregate (Fig. 12b, corresponding to IAG-Run27 in Tab. 1). Both P1 (light

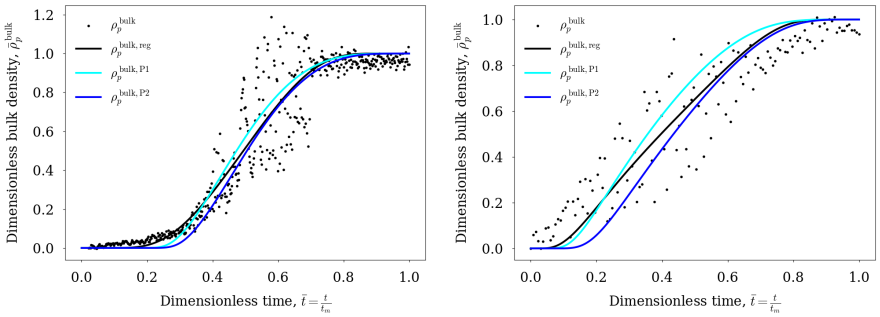

(a) TUDA - Run27 (light aggregate). (b) IAG - Run27 (dense aggregate).

FIGURE 12: Comparison between $\bar{\rho}_p^{\text{bulk,exp}}(t)$ and $\bar{\rho}_p^{\text{bulk}}(Y_l(t))$. Influence of the reconstructions P1 and P2. Test cases TUDA - Run27 and IAG - Run27 (Tab. 1)

blue solid line) and P2 (dark blue solid line) reconstructions are compared. For the light aggregate (Fig. 12a), both reconstructions P1 and P2 are accurate in accounting for the variation of $\bar{\rho}_p^{\text{bulk}}$ with time. For the dense aggregate, the most accurate reconstruction is P2. The conclusion is similar for all the snowflakes in Tab. 1 (Figs. A.16, A.17 and A.18).

5. Melting model : assessement and discussion

5.1. Prediction of the particle melting time

Melting times are compared between the *Mitra's* model (Sec. 4.1), which is the historical model for snowflake melting and will serve as a reference, the ρ_p^{core} model (Sec. 4.2) and the new ρ_p^{bulk} model (Sec. 4.3) with the two approaches P1 and P2 to compute $\bar{\rho}_p^{\text{bulk}}(Y_l)$. In Fig. 13, for each of the models, the melting times t_m^{num} (Y axis) are numerically estimated and compared to the experimental melting times t_m^{exp} (X axis) evaluated by the procedure in Sec. 3.2. Each symbol corresponds to a test case in Tab. 1. Green (resp. magenta, light blue and dark blue) color is for the *Mitra's* (resp. *ice core density based* ρ_p^{core}, *ice bulk*

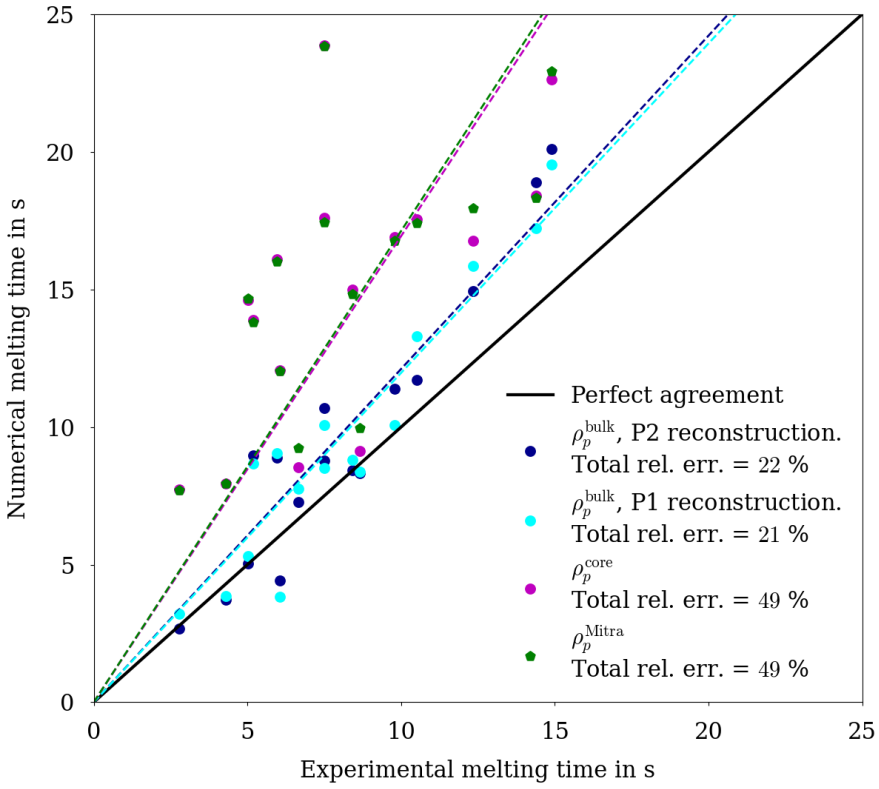

FIGURE 13: Melting times.

density based ρ_p^{bulk}) model. The black solid line indicates a perfect agreement (i.e. $t_m^{num} = t_m^{exp}$). The dashed lines correspond to the linear regressions derived for each of the models. The following error between t_m^{num} and t_m^{exp} is also given as an indication in Fig. 13 for each model :

$$err = \left(\frac{\sum_{i \in \mathcal{E}} \left[t_m^{num}(i) - t_m^{exp}(i) \right]^2}{\sum_{i \in \mathcal{E}} \left[t_m^{exp}(i) \right]^2} \right)^{1/2} \tag{40}$$

where $\mathcal{E}$ represents the set of snowflakes in Tab. 1. The new bulk density based model, whether using P1 or P2 approach, is on average more accurate in estimating the melting time of the snowflake (at least by a factor of 2). The accuracy of the core density based model is of the same order of magnitude as that of the historical *Mitra's* model. Thus the ρ_p^{core} model, initially developed for ice crystals of higher density than snowflakes, accurately addresses the melting of a snowflake, provided that the sphericity Φ_0 of the initial dry particle can be estimated and is not too low.

Suggestions for revisiting *Mitra's* model have also been tested. Firstly, in Eq. (22), regarding the definition of AR and ρ_p^{Mitra} as a function of Y_l, instead of considering constant values for the initial values $AR(0)$ and $\rho_p^{\text{Mitra}}(0)$ (0.3 and 20 kg.m^{-3} respectively, regardless of the shape of the dry particle), the values obtained from the spheroidal 2D-to-3D geometric reconstruction for the dry snowflake have been used (orange square symbols, and noted *Mitra revisited R1* in Fig. 14). Secondly, in addition to the previous assumption, the linear model for the evolution of the particle density with respect to Y_l (Eq. (22b)) has been replaced by the model $\rho_p^{\text{bulk}}(Y_l)$ (Eq. (32)) proposed in this manuscript (pink triangular symbol, and noted *Mitra revisited R2* in Fig. 14). We can see that considering the specific geometry of the dry snowflake only slightly improves the estimation of the melting time. On the other hand, the use of a more elaborate model for the particle density as a function of Y_l (here the bulk density ρ_p^{bulk}) significantly improves the estimation of the melting time for the *Mitra's* model (error decrease from 49% to 35%).

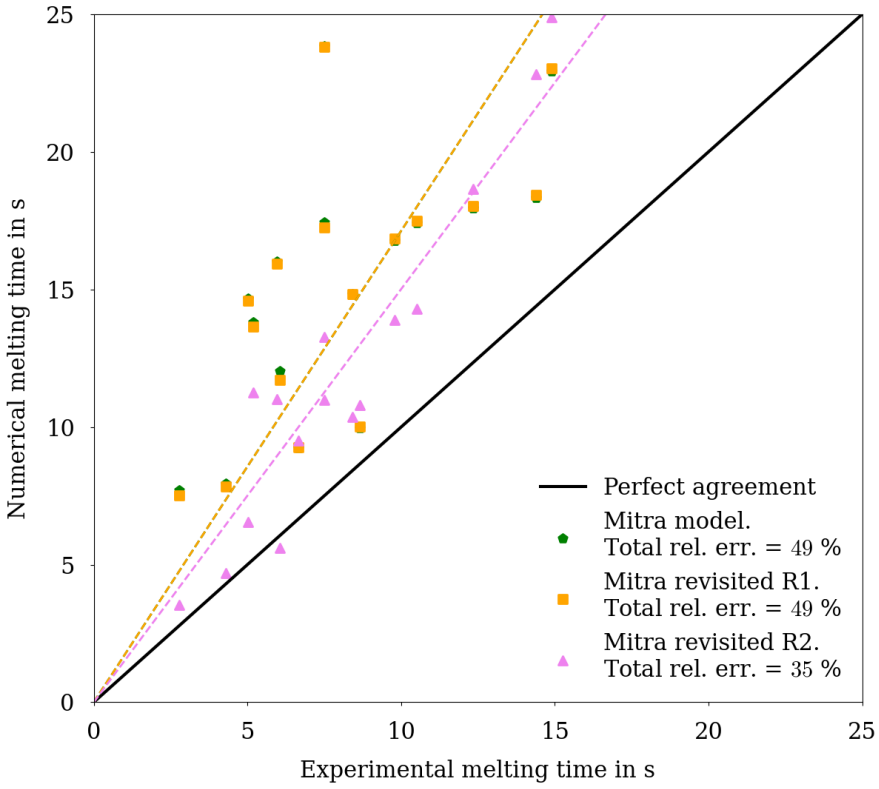

FIGURE 14: Revisited versions of the *Mitra's* model. Influence on the melting time.

5.2. Prediction of the particle liquid fraction (Y_l) evolution during the melting process

Figure 15 represents on the same plot the time evolution of Y_l (left axis) and of the dimensionless bulk density $\bar{\rho}_p^{\text{bulk}}$ (right axis) for each of the models. The black dashed curve refers to $\bar{\rho}_p^{\text{bulk,reg}}$ (Sec. 3.3) and is derived from the

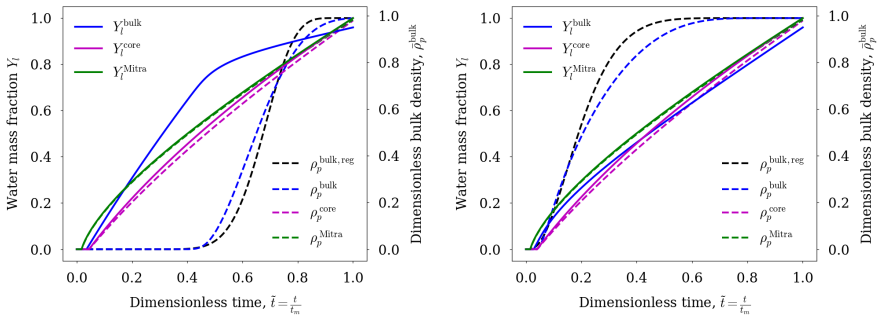

(a) TUDA - Run36 (light aggregate)

(b) TUDA - Run25 (dense aggregate)

FIGURE 15: Time evolution of Y_l (left axis) and ρ_p (right axis).

experiments. Y_l^{Mitra}, Y_l^{core} and Y_l^{bulk} denote the evolutions of Y_l obtained by the *Mitra's*, ρ_p^{core} and the new ρ_p^{bulk} models respectively. For the ρ_p^{bulk} model, only the P2 reconstruction is presented. Two representative test cases from Tab. 1 are selected for discussion : a light aggregate (TUDA - Run36, Fig. 15a) and a dense aggregate (TUDA - Run25, Fig. 15b).

For the light snowflake, only the ρ_p^{bulk} model clearly shows a two-slope evolution. At early times ($t/t_m < 0.4$ in Fig. 15a), the snowflake melts quickly with a rapid increase in Y_l. This step corresponds to the early times when the values of the bulk density remains close to those of the dry snowflake, for which the contact surface with the hot outer atmosphere is maximum, thus enhancing heat exchange and the melting of the snowflake. At later times ($t/t_m > 0.4$ in Fig. 15a), the snowflake melts not so fast with a slower evolution of Y_l up to 1. During this second step, the shape of the snowflake turns into that of a spherical particle with a smaller contact surface and thus a decrease in the dynamics

of the melting process. Thus, unlike *Mitra's* and ρ_p^{core} models, the ρ_p^{bulk} model proposed in this manuscript leads to a two-slope melting rate, first fast and then slower, which is in agreement with the description of the successive stages of the melting process of a light aggregate (Fig. 1).

For the dense agregate (Fig. 15b), the melting process starts directly at stage III, so the time evolution of Y_l is similar for the three models.

For the sake of completeness, the plots for all the cases of Tab. 1 are given in Figs. A.19 and A.20 for light aggregates, and in Fig. A.21 for dense aggregates. Conclusions are similar to the ones previously made.

6. Conclusions

In this paper, we compared three models to deal with the melting of a snowflake of arbitrary shape, namely two already existing models [16, 12] and a new model. Both the new model and the *Mitra's* model are based on a simple geometrical model of the snowflake (oblate enveloping spheroid) and on the notion of bulk density. This allows defining the heat flux exchanged between the air and the snowflake from only three parameters : the mass of the particle, its bulk density ρ_p^{bulk}, which corresponds (up to a multiplicative constant) to the ratio between the volume of the spheroid and the real volume of the snowflake, and the aspect ratio of the spheroid (or, which is equivalent, its sphericity). The third model (denoted by ρ_p^{core} model) is even simpler since it uses only two independent parameters : the mass of the snowflake (directly related to its real volume or equivalent volume diameter) and its real sphericity which allows deducing its exchange surface.

Regarding the prediction of the total melting time, we can clearly say that the new proposed model is more accurate than the existing models since its average relative error with respect to the experimental data is about 20% while it is more than 40% for the other two. Moreover, for light snowflakes, contrary to the model proposed by Mitra, the new model is able to account for the evolution in three phases (slow, fast, slow) of the bulk density as a function of time. This also

explains to a large extent its ability to predict more accurately the total melting time. To achieve this result, the key ingredient was the search for a non-linear (sigmoid) relationship between the bulk density of a snowflake and its liquid water fraction. In his model, Mitra had assumed an affine relationship which seems to be contradicted by our experimental results. As shown, it is possible to improve the accuracy of Mitra's model by replacing its affine relationship with the nonlinear relationship we have established. However, the estimate of total melting time still remains less accurate on average than with our new model.

Concerning the third model [12] which only uses the core density of the particle and its sphericity, its accuracy relies entirely on a correct estimation of the evolution of the sphericity of the snowflake during the melting process, since only this parameter allows us to take into account the effects related to the non-spherical shape. Once again, it seems that an affine relation between Φ and Y_l is not sufficient as soon as one is interested in light snowflakes with a very low initial sphericity (of the order of 0.1 to 0.2), which was not the case in the experimental study presented in [5]. Even if we have not tried to do so, we can think that the accuracy of the ρ_p^{core} model could be improved by replacing the affine relation between Φ and Y_l by a non-linear one.

To conclude, we can say first of all that our experimental study has confirmed Mitra's observations on the existence of several stages in the dynamics of the melting process of a snowflake. Moreover, in terms of modeling, we have exploited these observations to propose an empirical relation to link the bulk density of a melting snowflake to its liquid water fraction. Taking into account this highly non-linear relationship, we have proposed a new melting model capable of recovering the melting times of the 16 runs in our database with an average relative accuracy of 20%, which, given the uncertainties and simplifications inherent in this type of model, seems quite acceptable. In the future, it will be necessary to consolidate these results by continuing the validation of the model (and if necessary its improvement) using other experimental data.

Acknowledgments

The funding from the European Union's Horizon 2020 research and innovation program under grant agreement No 824310 is gratefully acknowledged. Airborne data used in this study were obtained using the aircraft managed by SAFIRE, the French facility for airborne research, a research infrastructure of the French National Center for Scientific Research (CNRS), Météo-France and the French National Center for Space Studies (CNES). The microphysical in situ data were collected using instruments from the French Airborne Measurement Platform, a facility partially funded by CNRS/INSU and CNES. The work of Pierre Trontin was partially supported by the LABEX iMUST of the University of Lyon (ANR-10-LABX-0064), created within the « Plan France 2030 » set up by the French government and managed by the French National Research Agency (ANR). We would like to thank Pierre Coutris for the definition, preparation and realization of the ICE GENESIS campaign and Louis Jaffeux for processing the PIP data.

Références

[1] J. Mason, W. Strapp, P. Chow, The ice particle threat to engines in flight, in : 44th AIAA Aerospace Sciences Meeting and Exhibit, 2006, p. 206. doi:10.2514/6.2006-206.

[2] U. Nakaya, T. Terada Jr, Simultaneous observations of the mass, falling velocity and form of individual snow crystals, Journal of the Faculty of Science, Physics 1 (7) (1935) 191–200.
URL http://hdl.handle.net/2115/34452

[3] H. R. Pruppacher, J. D. Klett, Microstructure of atmospheric clouds and precipitation, in : Microphysics of clouds and precipitation, Springer, 2010, pp. 10–73. doi:10.1007/978-0-306-48100-0_2.

[4] C. Praz, Y.-A. Roulet, A. Berne, Solid hydrometeor classification and riming degree estimation from pictures collected with a multi-angle snowflake

camera, Atmospheric Measurement Techniques 10 (4) (2017) 1335–1357. doi:10.5194/amt-10-1335-2017.

[5] T. Hauk, E. Bonaccurso, P. Villedieu, P. Trontin, Theoretical and experimental investigation of the melting process of ice particles, Journal of Thermophysics and Heat Transfer 30 (4) (2016) 946–954. doi:10.2514/1.T4886.

[6] E. Norde, J.-M. Senoner, E. T. A. van der Weide, P. Trontin, H. W. M. Hoeijmakers, P. Villedieu, Eulerian and lagrangian ice-crystal trajectory simulations in a generic turbofan compressor, Journal of propulsion and power 35 (1) (2019) 26–40. doi:10.2514/1.B36916.

[7] J.-M. Senoner, P. Trontin, L. Reitter, N. Karpen, M. Schremb, M. Vargas, P. Villedieu, Ice particle impact on solid walls : size modeling of reemited fragments, International Journal of Impact Engineering (2022) 104322doi:10.1016/j.ijimpeng.2022.104322.

[8] L. Reitter, H. Lohmann, M. Schremb, I. Roisman, J. Hussong, C. Tropea, Impact of an ice particle onto a dry rigid substrate : Dynamic sintering of a residual ice cone, Cold Regions Science and Technology 194 (2022) 103416. doi:10.1016/j.coldregions.2021.103416.

[9] P. Trontin, P. Villedieu, A comprehensive accretion model for glaciated icing conditions, International Journal of Multiphase Flow 108 (2018) 105–123. doi:10.1016/j.ijmultiphaseflow.2018.06.023.

[10] A. Baumert, S. Bansmer, P. Trontin, P. Villedieu, Experimental and numerical investigations on aircraft icing at mixed phase conditions, International Journal of Heat and Mass Transfer 123 (2018) 957–978. doi:10.1016/j.ijheatmasstransfer.2018.02.008.

[11] B. Mason, On the melting of hailstones, Quarterly Journal of the Royal Meteorological Society 82 (352) (1956) 209–216. doi:10.1002/qj.49708235207.

[12] P. Villedieu, P. Trontin, R. Chauvin, Glaciated and mixed phase ice accretion modeling using onera 2d icing suite, in : 6th AIAA atmospheric and space environments conference, 2014, p. 2199. doi:10.2514/6.2014-2199.

[13] N. Frossling, The evaporation of falling drops, gerlands beitr, Geophys. 52 (1938) 170–216.

[14] X. Yang, M. McGilvray, D. R. Gillespie, Modelling the particle trajectory and melting behaviour of non-spherical ice crystal particles, International Journal of Multiphase Flow 148 (2022) 103949. doi:10.1016/j.ijmultiphaseflow.2021.103949.

[15] T. Matsuo, Y. Sasyo, Empirical formula for the melting rate of snowflakes, Journal of the Meteorological Society of Japan. Ser. II 59 (1) (1981) 1–9. doi:10.2151/jmsj1965.59.1_1.

[16] S. Mitra, O. Vohl, M. Ahr, H. Pruppacher, A wind tunnel and theoretical study of the melting behavior of atmospheric ice particles. iv : Experiment and theory for snow flakes, Journal of the Atmospheric Sciences 47 (5) (1990) 584–591. doi:10.1175/1520-0469(1990)047<0584:AWTATS>2.0.CO;2.

[17] B. Aguilar, P. Trontin, L. Reitter, K. Köbschall, F. Dezitter, I. Roisman, P. Villedieu, Ice crystal drag model extension to snowflakes : Experimental and numerical investigations, AIAA Journal (2022) 1–14doi:10.2514/1.J062122.

[18] D. M. Kintea, T. Hauk, I. V. Roisman, C. Tropea, Shape evolution of a melting nonspherical particle, Physical review. E, Statistical, nonlinear, and soft matter physics 92 (3) (2015) 033012. doi:10.1103/PhysRevE.92.033012.

[19] Ice genesis : the next generation of 3d simulation means for icing, https://www.ice-genesis.eu/, accessed : 2022-10-01 (2019).

[20] B. Baker, R. P. Lawson, Improvement in determination of ice water content from two-dimensional particle imagery. part i : Image-to-mass relationships, Journal of applied meteorology and climatology 45 (9) (2006) 1282–1290. doi:10.1175/JAM2398.1.

[21] H. R. Pruppacher, J. D. Klett, Microphysics of Clouds and Precipitation : Reprinted 1980, Springer Science & Business Media, 2012. doi:10.1007/978-0-306-48100-0_2.

[22] P. Trontin, G. Blanchard, P. Villedieu, A comprehensive numerical model for mixed-phase and glaciated icing conditions, in : 8th AIAA Atmospheric and Space Environments Conference, 2016, p. 3742. doi:10.2514/6.2016-3742.

Annexe A. Additional figures

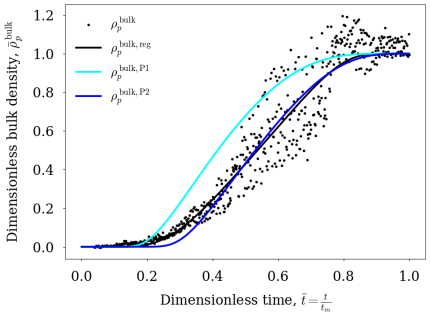

(a) TUDA - Run26

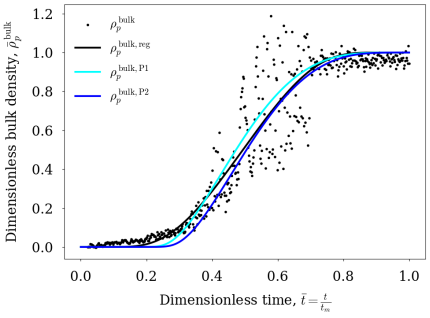

(b) TUDA - Run27

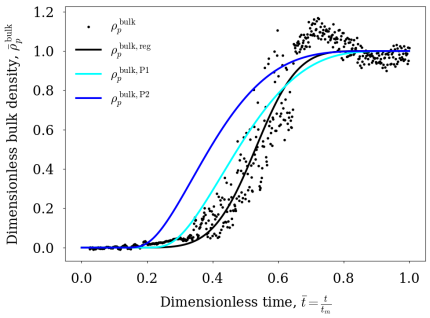

(c) TUDA - Run28

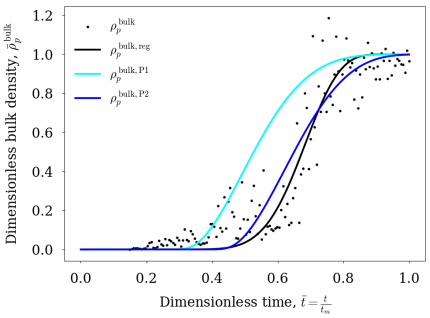

(d) TUDA - Run36

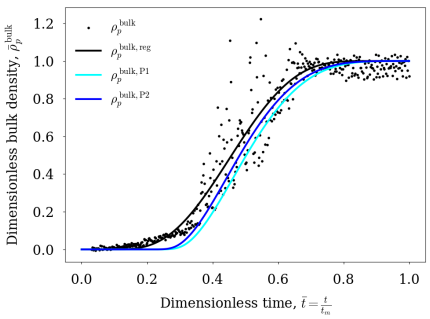

(e) TUDA - Run37

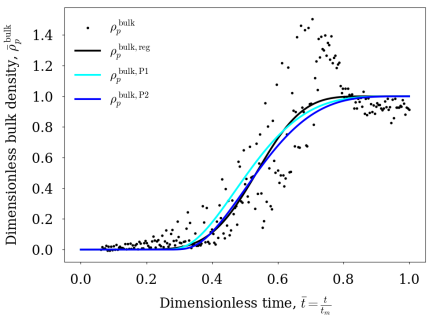

(f) TUDA - Run38

FIGURE A.16: Time evolution of the particle density ρ_p. Light aggregates (1/2).

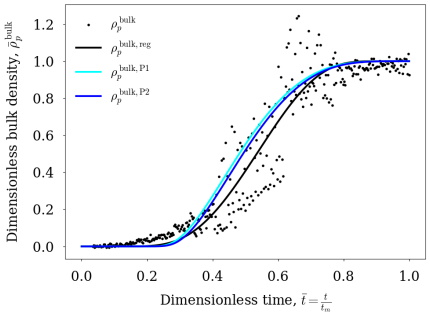

(a) TUDA - Run39

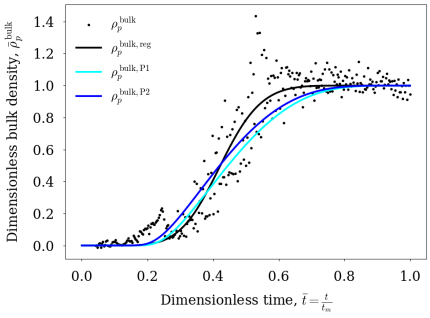

(b) TUDA - Run40

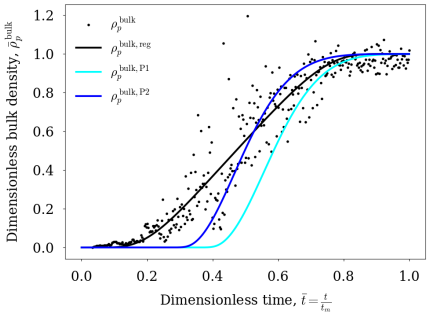

(c) TUDA - Run51

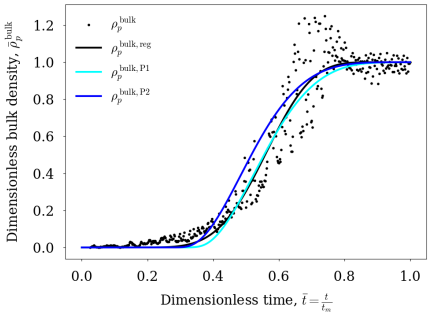

(d) TUDA - Run71

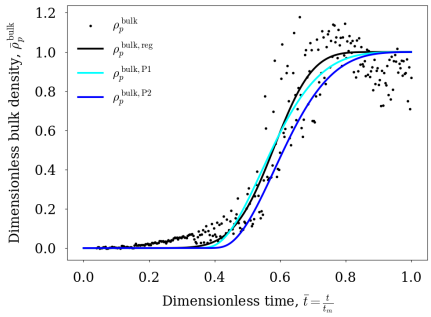

(e) TUDA - Run72

FIGURE A.17: Time evolution of the particle density ρ_p. Light aggregates (2/2).

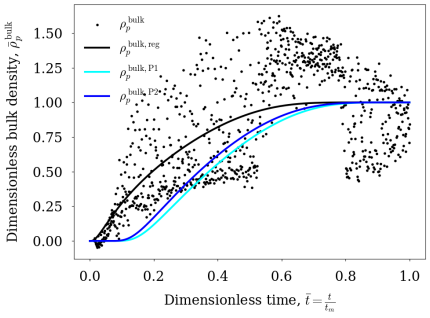

(a) TUDA - Run13

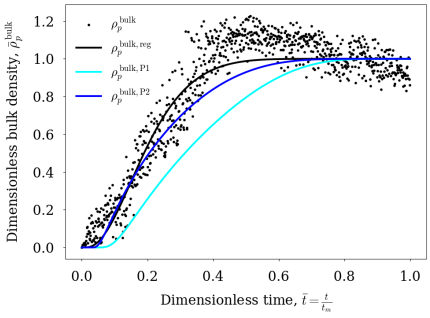

(b) TUDA - Run25

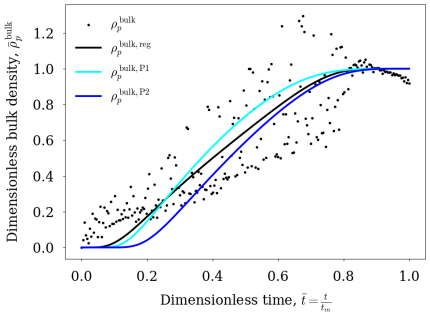

(c) IAG - Run18

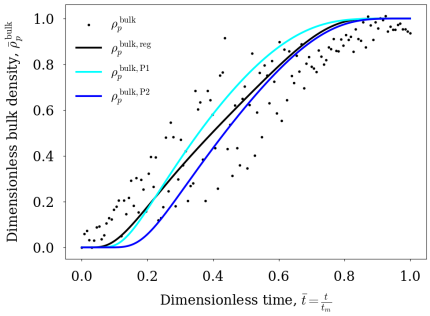

(d) IAG - Run27

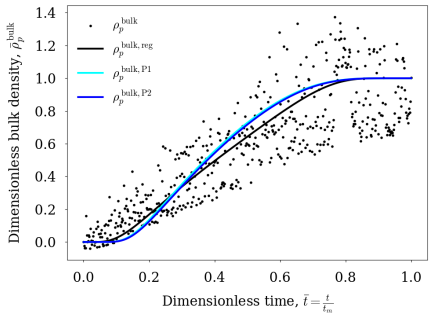

(e) IAG - Run38

FIGURE A.18: Time evolution of the particle density ρ_p. Dense aggregates.

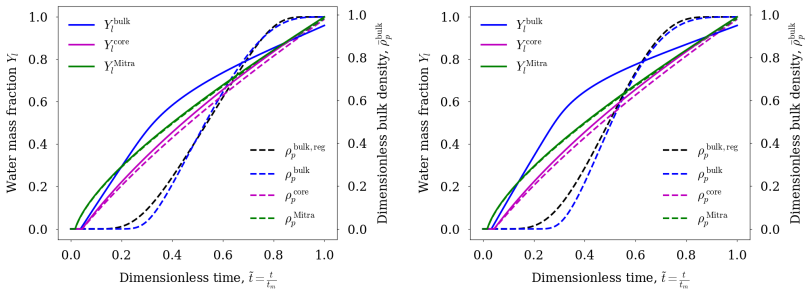

(a) TUDA - Run26

(b) TUDA - Run27

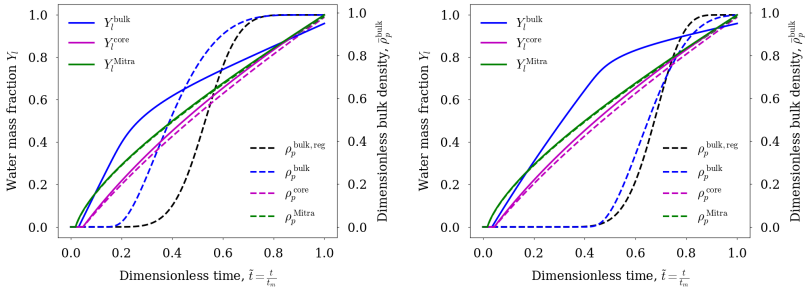

(c) TUDA - Run28

(d) TUDA - Run36

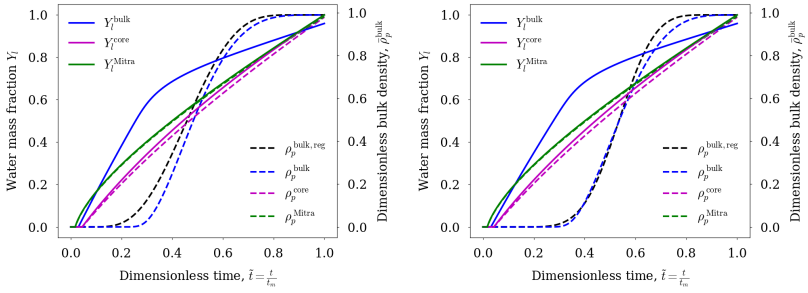

(e) TUDA - Run37

(f) TUDA - Run38

FIGURE A.19: Time evolution of the particle liquid mass fraction Y_l. As a reminder, time evolutions $\bar{\rho}_p^{\text{bulk,exp,reg}}(t)$ are recalled. Light aggregates (1/2).

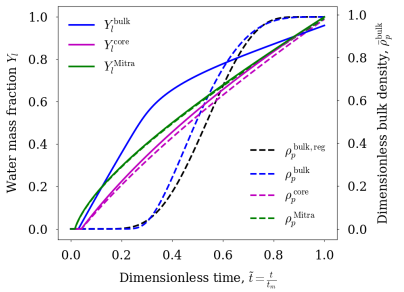

(a) TUDA - Run39

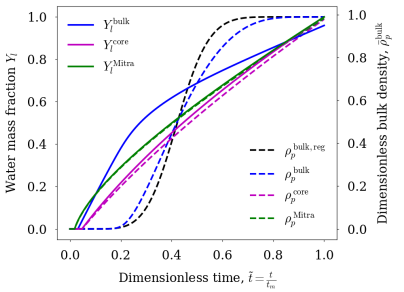

(b) TUDA - Run40

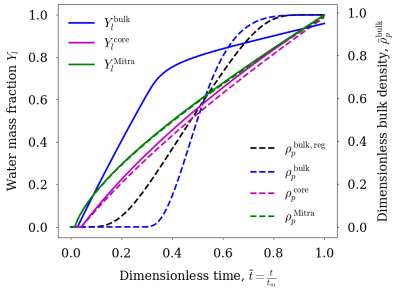

(c) TUDA - Run51

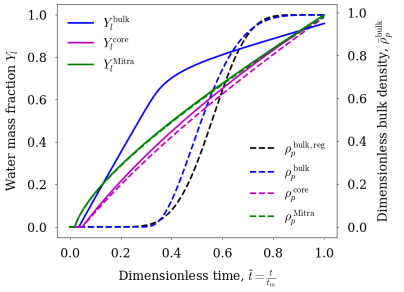

(d) TUDA - Run71

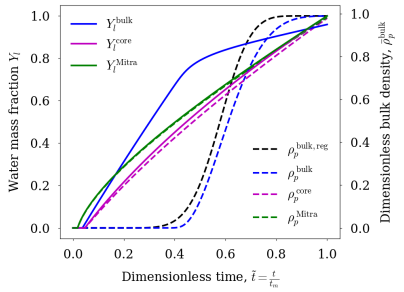

(e) TUDA - Run72

FIGURE A.20: Time evolution of the particle liquid mass fraction Y_l. As a reminder, time evolutions $\bar{\rho}_p^{\text{bulk,exp,reg}}(t)$ are recalled. Light aggregates (2/2).

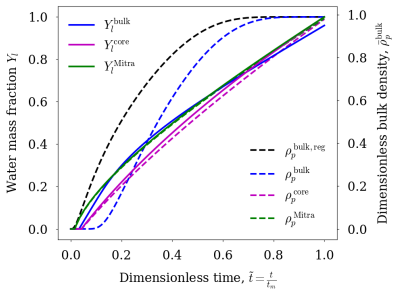

(a) TUDA - Run13

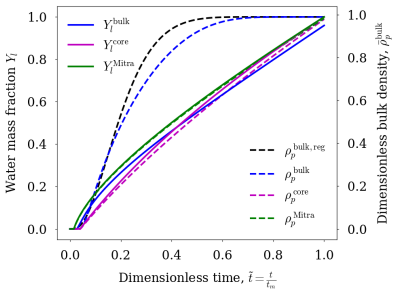

(b) TUDA - Run25

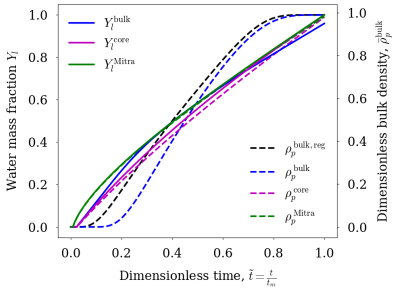

(c) IAG - Run18

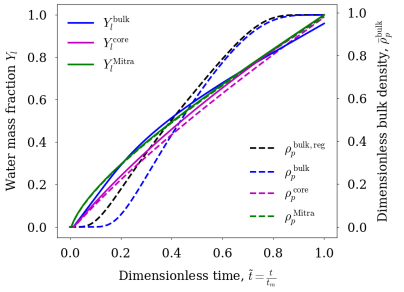

(d) IAG - Run27

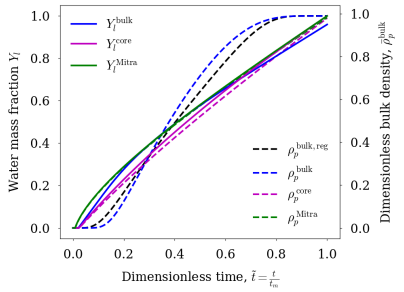

(e) IAG - Run38

FIGURE A.21: Time evolution of the particle liquid mass fraction Y_l. As a reminder, time evolutions $\bar{\rho}_p^{\text{bulk,exp,reg}}(t)$ are recalled. Dense aggregates.